Article

# Water Ligands Regulate the Redox Leveling Mechanism of the Oxygen-Evolving Complex of the Photosystem II

Jinchan Liu, Ke R. Yang, Zhuoran Long, William H. Armstrong, Gary W. Brudvig, and Victor S. Batista*

Read Online

ACCESS | 📊 Metrics & More | 📖 Article Recommendations | 🗎 Supporting Information

**ABSTRACT:** Understanding how water ligands regulate the conformational changes and functionality of the oxygen-evolving complex (OEC) in photosystem II (PSII) throughout the catalytic cycle of oxygen evolution remains a highly intriguing and unresolved challenge. In this study, we investigate the effect of water insertion (WI) on the redox state of the OEC by using the molecular dynamics (MD) and quantum mechanics/molecular mechanics (QM/MM) hybrid methods. We find that water binding significantly reduces the free energy change for proton-coupled electron transfer (PCET) from Mn to $Y_Z^\bullet$, underscoring the important regulatory role of water binding, which is essential for enabling the OEC redox-leveling mechanism along the catalytic cycle. We propose a water binding mechanism in which WI is thermodynamically favored by the closed-cubane form of the OEC, with water delivery mediated by $Ca^{2+}$ ligand exchange. Isomerization from the closed- to open-cubane conformation at three post-WI states highlights the importance of the location of the $Mn^{III}$ center in the OEC and the orientation of its Jahn−Teller axis to conformational changes of the OEC, which might be critical for the formation of the O−O bond. These findings reveal a complex interplay between conformational changes in the OEC and the ligand environment during the activation of the OEC by $Y_Z^\bullet$. Analogous regulatory effects due to water ligand binding are expected to be important for a wide range of catalysts activated by redox state transitions in aqueous environments.
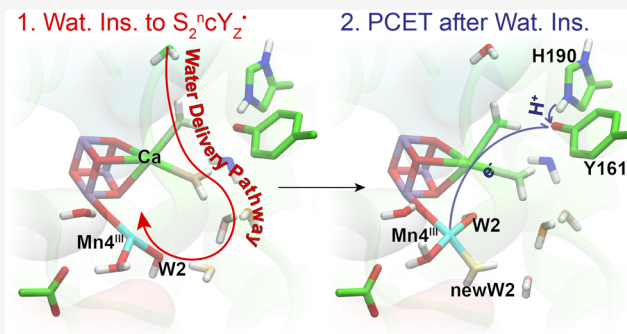
## INTRODUCTION

The oxygen in the Earth's atmosphere has been generated by photosynthetic organisms and sustains all forms of aerobic life. Photosynthetic oxygen evolution involves water oxidation catalyzed by photosystem II (PSII), a protein complex embedded in the thylakoid membrane of green plant chloroplasts (or internal membranes of cyanobacteria) (Figure 1A).[1−5] Water is oxidized at the oxygen-evolving complex (OEC) of PSII, an oxo-bridged $Mn_4Ca$ metal complex coordinated by amino acid ligands and water molecules (W1−W4) (Figure 1B,C).[4−8] The OEC catalyzes the reaction $2H_2O \rightarrow 4H^+ + 4e^- + O_2$, after evolving through the redox state intermediates of the catalytic cycle proposed by Joliot and Kok, which was then extended by Klauss et al. (Figure 1D). Along this cycle, the OEC is progressively oxidized, evolving through five "storage" (S) redox states, denoted as $S_i$ ($i = 0−4$), where $i$ represents the number of stored oxidizing equivalents (i.e., missing electrons or holes). Such accumulation of oxidizing equivalents is driven by solar photo-absorption by the specialized chlorophyll $a$ species, P680. The excited singlet state of P680 decays to the oxidized state $P680^+$ upon electron transfer to a nearby pheophytin (Pheo). The electron is then transferred from Pheo to a primary quinone electron acceptor ($Q_A$) and then to a secondary plastoquinone electron acceptor ($Q_B$), which functions as a two-electron

carrier and forms plastohydroquinone ($PQH_2$) upon two-electron reduction and protonation with protons from the stromal side of the membrane.[9] The oxidized chlorophyll $a$ species, $P680^+$, oxidizes tyrosine Z, $Y_Z$ (D1-Y161) next to the OEC, forming the $Y_Z^\bullet$ radical coupled to proton transfer to H190.[10,11] The $Y_Z^\bullet$ functions as an effective primary oxidant by oxidizing the OEC with a narrow range of redox potentials, getting the proton transferred to H190 back.[10,12−14] After four iterations of such a proton-coupled redox process, the OEC has accumulated four oxidizing equivalents so it can extract four electrons from two substrate water molecules to produce dioxygen. An outstanding challenge is to understand the intricate mechanism leading to substrate water binding to the OEC and water oxidation catalyzed by the oxidized form of the OEC,[15,16] a process that could provide valuable insights for the design of artificial catalytic water-splitting technologies.
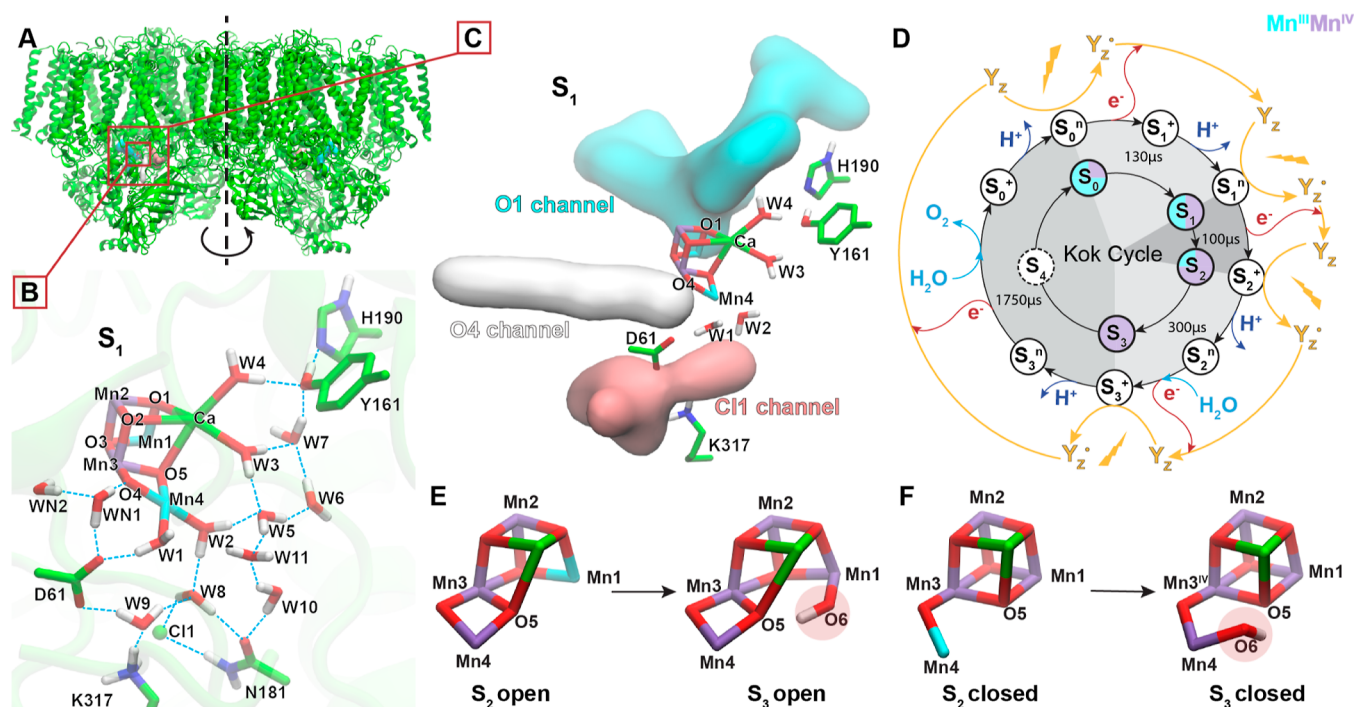
**Figure 1.** Oxygen-evolving complex (OEC) of (A) the photosystem II (PSII) protein dimer rendered in green. (B) The OEC at the dark-stable $S_1$ state optimized from PDB3WU2. The OEC is composed of 4 high valence Mn, a Ca, and 5 $\mu$-oxo bridges, and its surrounding environment with waters forming an extensive hydrogen bond network. W1−W4 are water ligands directly coordinated to the OEC, while W5−W11 are connected to amino acid residues and a Cl$^-$ ion. See Table S4 for the naming of water molecules in other work. (C) Three water channels ending at the OEC, with the O1 channel in cyan, the O4 channel in light gray, and the Cl1 channel in pink. (D) Catalytic cycle of the OEC, where the OEC cluster is oxidized stepwise by $Y_Z^\bullet$, and oxidizing equivalents are accumulated in five "storage" states ($S_0$–$S_4$). These storage states are further subdivided based on the stepwise electron transfer to $Y_Z^\bullet$ and proton exiting PSII, where the charge of the OEC cluster, including the water substrates, alters between positive (+) and neutral (n). (E) The low-spin open-cubane conformation at $S_2$, which is proposed to give rise to the $g = 2.0$ multiline EPR signal (left) and its subsequent $S_3$ state (right) with an extra ligand inserted to Mn1. (F) The computationally derived closed-cubane conformation at $S_2$ (left), which is proposed to give rise to the $g = 4.1$ EPR signal and its subsequent $S_3$ state (right) with an extra ligand inserted to Mn4. Mn$^{III}$ is colored in cyan and Mn$^{IV}$ in purple, which is consistently applied in all subsequent figures.

The OEC is embedded in the D1 protein subunit of PSII, so the substrate water molecules must be delivered from the lumen. Three channels that may deliver water from the lumen to the OEC have been identified nowadays called the Cl1 channel, the O1 channel, and the O4 channel.[17−19] The O1 channel approaches a water ligand of Ca and the Cl1 channel as well as the O4 channel approaches the water ligands of the dangling Mn4 (Figure 1C).[20] Water molecules bind to the OEC most likely during the $S_2 \rightarrow S_3$ and $S_3 \rightarrow S_0$ transitions, respectively.[21,22] These transitions have been investigated by water exchange experiments, where $^{18}$O-labeled water yields labeled dioxygen that is monitored by mass spectrometry as a function of time.[23,24] However, the interpretation of these experiments remains the subject of debate, leaving uncertain the nature of the delivery mechanism and identity of substrate water molecules.[25−27]

The mechanism of water delivery during the $S_2 \rightarrow S_3$ transition has been studied quite extensively through the analysis of the structures of $S_2$ and $S_3$ states.[28−37] The $S_2$ state, characterized by three Mn$^{IV}$ ions and a Mn$^{III}$ ion, exhibits two distinct EPR signals: a multiline EPR signal centered at $g = 2.0$[38] and another signal centered at $g = 4.1$.[39] The $g = 2.0$ signal is attributed to a low-spin open-cubane conformation with O5 coordinating to Mn4, resulting in six-coordinated Mn4$^{IV}$ and five-coordinated Mn1$^{III}$.[40−42] Such an open-cubane conformer was proposed to proceed to its subsequent $S_3$ open-cubane state, with an extra ligand added to Mn1 to complete a coordination number of six for all four Mn (Figure 1E).[43−46] The insertion of this extra ligand, now widely accepted as a OH$^-$ and named O6, is supported by EPR experiments, suggesting that all four Mn$^{IV}$ ions have six ligands in the $S_3$ state,[47] together with X-ray free electron laser (XFEL) crystallography densities indicating a ligand insertion to the open-cubane $S_2$.[35−37] In comparison, the origin of the $g = 4.1$ signal is more contentious. A closed-cubane isomer, with O5 coordinating to Mn1 and Mn4 being five-coordinated, was first proposed theoretically by Pantazis et al.[40] The isomer is further adapted by other computational groups and proposed to proceed to its subsequent $S_3$ state with a OH$^-$ inserted to Mn4 (Figure 1F).[41−46,48] One piece of experimental evidence supporting the closed-cubane structure is the zero-field splitting (ZFS) tensor ascribed to the direction of Mn4, indicating Mn4 is trivalent in the $S_2$ high-spin state.[49] However, the lack of observed closed-cubane structures in XFEL crystallography densities obscures the origin of the $g = 4.1$ signal.[35−37] Two new open-cubane models, one with early ligand binding[50] and another one with O4 protonated[51,52] have been proposed to be responsible for the $g = 4.1$ signal. Despite the two new open-cubane structures proposed to give rise to the $g = 4.1$ EPR signal, which are also consistent with XFEL studies, many theoretical mechanisms still adopt the closed-cubane structure, underscoring the ongoing debate over the conformation responsible for the $g = 4.1$ signal.[48,53−58]
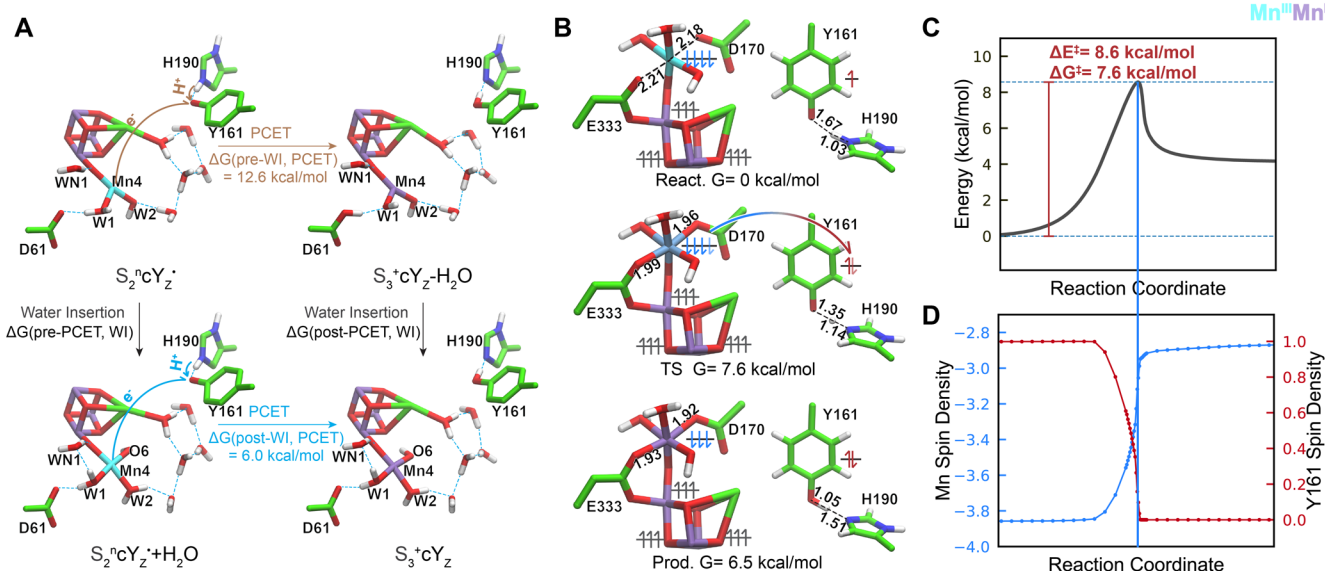
**Figure 2.** Potential pathways for transition from $S_2^n Y_Z^\bullet$ to $S_3^+ Y_Z$, which involves the electron transfer from $Mn4^{III}$ to $Y_Z^\bullet$ coupled by proton transfer from H190 to $Y_Z^\bullet$ and the water insertion (WI) to the OEC. (A) Thermodynamic cycle with the closed-cubane conformation that starts from $S_2^n Y_Z^\bullet$ ($S_2^n cY_Z^\bullet$) and concludes at $S_3^+ Y_Z$ ($S_3^+ cY_Z$). Without the WI, the free energy difference of the PCET is 12.6 kcal/mol, while it is reduced to 6.0 kcal/mol with the water inserted first. The WI lowers the free energy difference for the electron transfer by 6.6 kcal/mol, which suggests the regulatory role of WI on the relative reduction potential between $Y_Z^\bullet$ and $Mn4^{III}$. Calculations in this panel are done with all spins aligned as the high spin state. (B) PCET reaction post WI with a Mn spin configuration $\alpha\alpha\alpha\beta$, as indicated by up and down arrows. The process is characterized by elimination of the D170-Mn4-E333 Jahn−Teller axis when $Mn4^{III}$ is oxidized to $Mn4^{IV}$ and a proton traveling from NE2-H190 to OH−Y161, with a free energy barrier of 7.6 kcal/mol. (C) Energy of the cluster along the intrinsic reaction coordinate (IRC) path. (D) Mulliken spin population on Mn4 and $Y_Z^\bullet$ along the IRC path.

Although only the open-cubane is observed by XFEL crystallography, the interpretation of XFEL data remains debatable,[59−62] with the oxidation state of Mn in XFEL studies highly questioned[63] and a mixture of different populations at one snapshot not resolved.[64] Therefore, the existence of the closed-cubane isomer and its use to insert the sixth ligand cannot be ruled out. Extensive computational studies have proposed mechanisms for water insertion (WI) into both the open- and closed-cubane conformations during the $S_2 \rightarrow S_3$ state transition. One set of models includes the carousel and pivot mechanisms suggesting that W2 gets deprotonated and becomes integrated into the closed-cubane $S_2$ structure,[30,31,65−67] as well as some other mechanisms suggesting W3 binds to the closed-cubane.[29,48,58] These mechanisms are supported by Shoji et al. indicating WI to a closed-cubane conformation is more energetically favorable.[29] Another set of models suggests an open-cubane conformation can be used for ligand insertion.[68,69] In summary, it remains an open question as to whether water binds to the open-cubane or closed-cubane conformation.

The $S_2 \rightarrow S_3$ state transition involves an early deprotonation of the OEC, likely induced by the oxidation of $Y_Z$.[8,12,70] Binding of a water ligand could complete the coordination sphere of a five-coordinated $Mn^{III}$ and facilitate the $Mn^{III} \rightarrow Mn^{IV}$ oxidation by the $Y_Z^\bullet$ radical, resulting in an OEC structure with four hexacoordinated $Mn^{IV}$ centers.[35,37,43] Whether this is the actual sequence of events during the $S_2 \rightarrow S_3$ transition, however, remains controversial and is the subject of our study. The existence of an intermediate $S_3$ state featuring a five-coordinate $Mn^{IV}$ center has been proposed,[30] implying that $Y_Z^\bullet$ oxidizes a $Mn^{III}$ center before WI. Similarly, XFEL structures have suggested that the $Mn^{III} \rightarrow Mn^{IV}$ transition precedes[37] or is correlated with WI.[35] However,

the kinetics of $Y_Z^\bullet$ reduction indicate that $Mn^{III}$ is oxidized at the end of the $S_2 \rightarrow S_3$ transition.[8,71] Furthermore, Sakamoto et al. identified an early change in the hydrogen bond network,[33] attributed to WI before the oxidation of $Mn^{III}$ by $Y_Z^\bullet$.

Various mechanisms have been proposed for water binding leading to the formation of an O6 ligand, most of which fall into two categories. The first set of models proposes that O6 originates from W3,[29,34,48,68,69,72] which is bound to $Ca^{2+}$, a mechanistic hypothesis supported by the observation that replacing $Ca^{2+}$ with $Sr^{2+}$ changes the bending mode of a water ligand proposed to be deprotonated during the $S_2 \rightarrow S_3$ transition.[73] XFEL data, obtained after one or two flashes, was also utilized to investigate the $S_2 \rightarrow S_3$ transition. The analysis indicated that water molecules in the O1 channel exhibit increased mobility. This suggests that the O1 channel delivers W3 from the external aqueous environment to the OEC. Water in the vicinity of E189 has been proposed as an alternative origin of the ionization of O6. Binding that molecule to the OEC should require a rotation of the water around $Ca^{2+}$, similarly to the proposed rearrangement of W3 mechanism.[37] An alternative set of models suggested that O6 is formed from W2,[30,31,65−67] part of a so-called carousel or pivot process that is accompanied by movement of a water molecule in the O4 channel. This hypothesis is partially supported by the observation that mutating the serine 169 of D1 subunit (S169), anchoring WN1 situated at the O4 channel, to alanine results in an EPR spectrum interpreted as an early substrate water binding.[74,75]

To elucidate these unresolved questions, we employ density functional theory (DFT)-quantum mechanics/molecular mechanics (QM/MM) calculations to explore the potential intermediate states arising during the $S_2 \rightarrow S_3$ transition.

Starting with the $S_2^n Y_Z^\bullet$ state, we compare two pathways, including one with WI preceding Mn-oxidation and another one where Mn-oxidation occurs first. Our results suggest that WI is more likely to precede Mn-oxidation. Additionally, when comparing the closed-cubane and open-cubane structures, our calculations indicate that incorporating a water molecule into the closed-cubane state is energetically more favorable, which is further supported by our analysis of the S169A mutant. Utilizing transition state searching with DFT-QM/MM and the analysis of water mobility with molecular dynamics (MD), we found a mechanism that could lead to efficient water delivery to the closed-cubane state. Furthermore, we investigate the interconvertibility between the closed- and open-cubane states. Combining all of these calculations, we construct a detailed atomic-level model of the $S_2 \rightarrow S_3$ transition that could prepare the OEC for subsequent oxidation and O−O bond formation.

## ■ RESULTS

**Water Insertion during the $S_2 \rightarrow S_3$ Transition Promotes $Y_Z^\bullet$ Oxidizing $Mn^{III}$.** Our studies build upon previously reported $S_2$ open-cubane structures by Yang et al., with W1 = $H_2O$ sharing a proton with D61 and W2 = $H_2O$, consistent with the proton hyperfine coupling constants.[42] Based on such a $S_2^+ Y_Z$ structure, we posit an early stage proton removal during the $S_2 \rightarrow S_3$ transition, considering the photothermal beam deflection (PBD) experiments.[8] We propose that during the $S_2 \rightarrow S_3$ transition, the formation of $Y_Z^\bullet$ initiates a hydrogen bond network change, triggering a proton removal from W2. This first step yields W2 as a hydroxide ion ($OH^-$), which evolves into the O6 forming a hydrogen bond with O5 at $S_3$ state.[76] To advance to the $S_3$ state after the deprotonation, two subsequent processes are required: the oxidation of $Mn^{III}$ by $Y_Z^\bullet$, which simultaneously extracts a proton from H190—a proton-coupled electron transfer (PCET) reaction—and the incorporation of water into the OEC.

To delineate the sequence and intricacies of these events, we conducted QM/MM calculations. We computed the free energy changes associated with the PCET from $Mn^{III}$ to $Y_Z^\bullet$ before and after WI to the OEC by preparing four representative states as follows (Figure 2A): the initial state, $S_2^n Y_Z^\bullet$, was optimized based on the $S_2$ structures from Yang et al.[42] by deleting a proton on W2 and reorganizing the related hydrogen bond network, followed by its PCET product without WI, $S_3^+ Y_Z - H_2O$. Another state introduced water to $S_2^n Y_Z^\bullet$, yielding $S_2^n Y_Z^\bullet + H_2O$, which then proceeded to the final state, $S_3^+ Y_Z$, through PCET. These four states depict a thermodynamic cycle that starts from $S_2^n Y_Z^\bullet$ and concludes at $S_3^+ Y_Z$ via two pathways: WI first, followed by the post-WI PCET via $S_2^n Y_Z^\bullet + H_2O$ (WI-first), or the pre-WI PCET followed by WI via $S_3^+ Y_Z - H_2O$ (PCET-first).

We considered the possibility of three different isomers going through such a thermodynamic cycle: the open-cubane isomer giving rise to the $g = 2.0$ signal, and another two isomers possibly giving rise to the $g = 4.1$ high spin signal: the closed-cubane proposed by Pantazis et al.[40] and the protonation isomer of the open-cubane proposed by Corry and O'Malley.[51] The last isomer has O4 protonated and W2 deprotonated compared to a standard open-cubane, and here we name it the O4H open-cubane isomer. We optimize the three isomers at $S_2^+ Y_Z$ state with our QM/MM model (Figure S1), with the hydrogen bond network of lowest energy to our

knowledge (Figures S2 and S3). The open-cubane and the closed-cubane are almost iso-energetic, with the open-cubane being more favorable by 0.4 kcal/mol in free energy, consistent with previous calculations.[42] However, the O4H open-cubane is 14.9 kcal/mol higher in free energy, and therefore, we think it may not be stable enough to be present. This substantial energy increase of 14.9 kcal/mol can be attributed to protonation of a $\mu$-oxo bridge of $Mn^{IV}$ being very unfavorable, as suggested by Tagore et al.[77] Changes in hydrogen bond networks resulting from the change in protonation states are also likely to contribute to the increase in free energy (Figure S2). Such an unstable isomer proposed to give rise to the $g = 4.1$ signal intensity should be more stable under lower pH when its $\mu$-oxo bridge is protonated. However, this disagrees with the fact that the $g = 4.1$ signal can be enhanced when the pH is higher.[78] Considering that the O4H open-cubane isomer is energetically unfavorable and inconsistent with the experiment, we exclude it from our calculations and only consider the unprotonated open- and closed-cubane states for the thermodynamic cycle, denoted as the open- and closed-cubane states.

We optimized the four states of the thermodynamic cycle for both the open-cubane and the closed-cubane states, denoted with adding an "o" or "c" in the original name of the state. The structures are first optimized with all spins aligned as the high spin state: for the systems with a $Y_Z^\bullet$, the spin state is denoted as $\alpha\alpha\alpha\alpha\alpha$, where the first four letters represent the spin states for Mn1−4 and the last for $Y_Z^\bullet$. For the systems with $Y_Z$, the spin state is denoted as $\alpha\alpha\alpha\alpha$, representing Mn1−4. The spin configurations with $\alpha\alpha\alpha\beta$ and $\alpha\beta\alpha\beta$ for the four Mn ions were also explored and presented similar structures and energies compared to the high spin state (Tables S5 and S6). For conciseness, the high spin state will be used to represent the states unless otherwise specified. Structurally, pre-WI states, $S_2^n Y_Z^\bullet$ and $S_3^+ Y_Z - H_2O$ feature W2 as $OH^-$, while post-WI states, $S_2^n Y_Z^\bullet + H_2O$ and $S_3^+ Y_Z$ exhibit O6 as $OH^-$ and W2 as $H_2O$. The difference in the protonation states of W2 results in different hydrogen bond networks: in the pre-WI states, W2 accepts a hydrogen bond from W10, whereas it donates a hydrogen bond to W10 as a $H_2O$ in the post-WI states. For both of the pre-WI states, we adopted the hydrogen bond network of the lowest energy to our knowledge to represent the state (Figure S3), while post-WI states adopt the hydrogen bond network of the respective pre-WI states.

To verify our optimized structures, we simulated the extended X-ray absorption fine structure (EXAFS) spectrum of the $S_3^+ Y_Z$ states we optimized,[43] $S_3^+ oY_Z$ and $S_3^+ cY_Z$, since $S_3^+ Y_Z$ is a stable state capturable by experiment.[79] The simulated spectrum is in fair agreement with the spectrum produced experimentally (Figure S4). With the verified structures, we note that for the closed-cubane conformation, the free energy change for the pre-WI PCET from $S_2^n cY_Z^\bullet$ to $S_3^+ cY_Z - H_2O$ $[\Delta G(\text{pre-WI, PCET})]$ is 12.6 kcal/mol. With water, the $\Delta G(\text{post-WI, PCET})$ from $S_2^n cY_Z^\bullet + H_2O$ to $S_3^+ cY_Z$ is reduced to 6.0 kcal/mol, highlighting the regulatory role of WI in tuning the relative reduction potential between $Y_Z^\bullet$ and $Mn4^{III}$. Presumably, the added water ligand donates extra electron density to $Mn4^{III}$, thereby facilitating Mn-oxidation by lowering the reduction potential of $Mn4^{III}$. Without the extra water ligand inserted first, a less favorable five-coordinated $Mn4^{IV}$ is generated, underscoring the importance of WI as a prerequisite for PCET in favor of the WI-first pathway.

To extend our understanding from thermodynamics to the kinetics of the PCET, we performed a transition state search for the post-WI PCET with a spin configuration of $\alpha\alpha\alpha\beta\alpha$. This search yielded an energy barrier of 7.6 kcal/mol, corresponding to a time scale of 38 ns according to the Eyring equation, which captured both the electron transfer from Mn4 to $Y_Z^\bullet$, and the proton transfer from H190 to $Y_Z^\bullet$ (Figure 2B,C). On the electron donor side, Mn4 is oxidized from $Mn^{III}$ to $Mn^{IV}$, accompanied by notable changes in metal–ligand distances. Specifically, in the reactant, the Mn4-D170OD1 and Mn4-E333OE1 distances were initially 2.18 and 2.21 Å, shortened to 1.96 and 1.99 Å in the transition state, and finally settled at 1.92 and 1.93 Å, respectively. Thus, the Jahn–Teller elongation along the D170-Mn4-E333 axis was lost, as expected for the conversion of $Mn^{III}$ to $Mn^{IV}$. On the electron acceptor side, the $Y_Z^\bullet$ receives an electron from Mn4 and a proton from H190, which causes an increase in its CZ−OH bond from 1.28 to 1.35 Å. Additionally, the proton being transferred is situated 1.14 Å from NE2-H190 and 1.35 Å from OH−Y161 at the transition state.

For the open-cubane structures, we successfully optimized $S_2^n oY_Z^\bullet$, $S_2^n oY_Z^\bullet + H_2O$, and $S_3^+ oY_Z$ to their respective local minima (Figure S5 and Table 1). However, no local minimum

**Table 1. Relative Free Energy of the Four States, $S_2^n Y_Z^\bullet$, $S_3^+ Y_Z−H_2O$, $S_2^n Y_Z^\bullet + H_2O$, and $S_3^+ Y_Z$ for the Closed-Cubane and the Open-Cubane Conformers**

| QM size | system | closed | open |
|---|---|---|---|
| 213 atoms | $S_2^n Y_Z^\bullet$ | 0.0 | −3.0 |
| | $S_3^+ Y_Z−H_2O$ | 12.6 | N.A. |
| 216 atoms | $S_2^n Y_Z^\bullet + H_2O$ | 0.0 | +11.3 |
| | $S_3^+ Y_Z$ | 6.0 | 1.9 |

was identified for $S_3^+ oY_Z−H_2O$, which can be attributed to the charge environment of $Mn1^{IV}$ in the open-cubane. With negative charges coming from two carboxylate and two $\mu$-oxo ligands, the ligand environment is not negative enough to stabilize a five-coordinated $Mn^{IV}$ center. In contrast, $Mn4^{IV}$ in the closed-cubane is coordinated by two carboxylate groups, one $\mu$-oxo bridge and two $OH^-$, summing up to one more ligand of negative charge stabilizing the $Mn4^{IV}$. This lack of stability for $S_3^+ oY_Z−H_2O$ suggests the reduction potential for five-coordinated $Mn1^{IV}$ is so high that it is not sufficiently stable to manifest, making $\Delta G$(pre-WI, PCET) exceedingly high for the open-cubane. Given that the $\Delta G$(post-WI, PCET) for the open-cubane is −9.4 kcal/mol, this aligns seamlessly with observations concerning the closed-cubane, wherein WI promotes $Y_Z^\bullet$ oxidizing $Mn^{III}$.
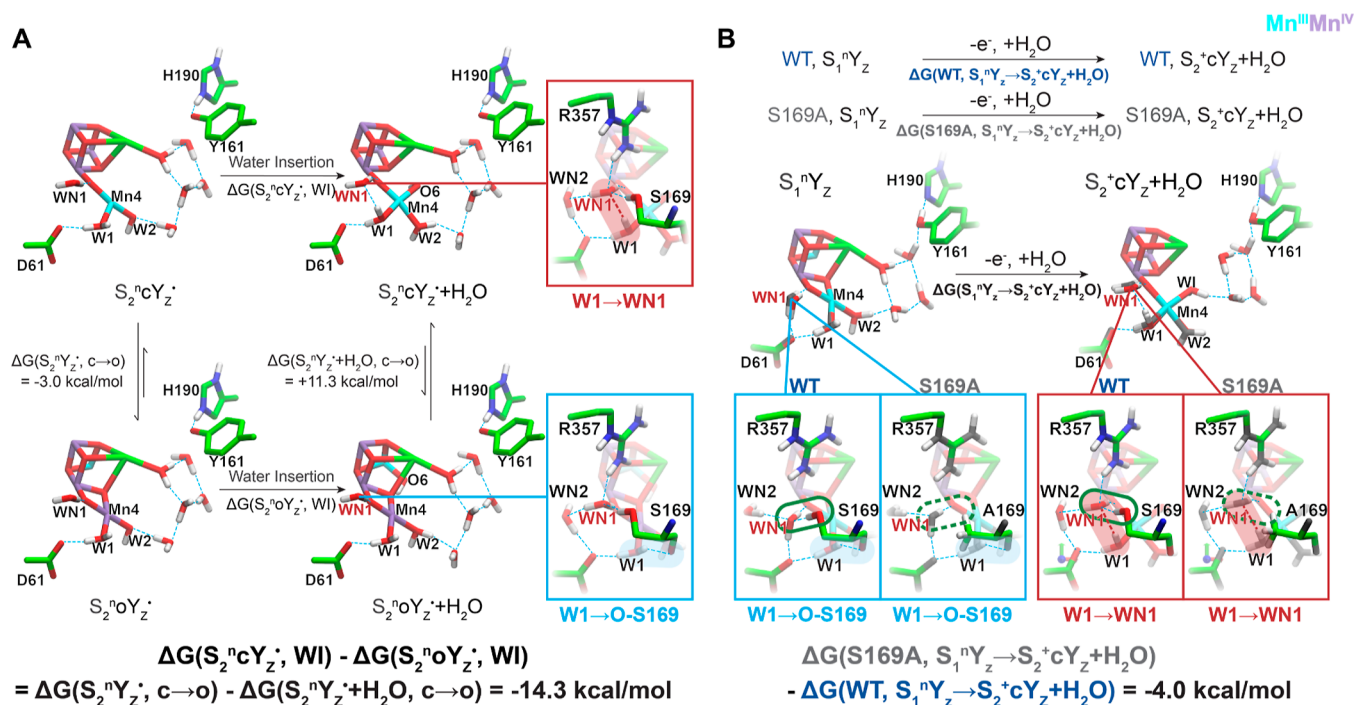
**Closed-Cubane of $S_2^n Y_Z^\bullet$ Is More Favorable for Water Insertion.** With the established understanding that WI promotes PCET, we aim to discern whether the closed-cubane or open-cubane is more conducive for WI. When comparing the structures of the $S_2$ states (Figure 3A), the hydrogen bond network for the closed-cubane and the open-cubane at the $S_2^n Y_Z^\bullet$ states is identical. Energetically, $S_2^n oY_Z^\bullet$ is more favorable than $S_2^n cY_Z^\bullet$ by 3.0 kcal/mol ($\Delta G(S_2^n Y_Z^\bullet$, c → o) = −3.0 kcal/mol), consistent with results from Yang et al.[42] and Bovi et al.[48] In contrast, upon WI, $S_2^n oY_Z^\bullet + H_2O$ is less favorable by 11.3 kcal/mol compared to $S_2^n cY_Z^\bullet + H_2O$ ($\Delta G(S_2^n Y_Z^\bullet + H_2O$, c → o) = 11.3 kcal/mol). This significant shift in energetic favorability amounts to a free energy difference of 14.3 kcal/

mol for WI between the two states and positions the $S_2^n cY_Z^\bullet$ state as the more viable candidate for WI.

The significant 14.3 kcal/mol of free energy difference in WI primarily arises from the fact that $S_2^n oY_Z^\bullet + H_2O$ is less favorable than $S_2^n cY_Z^\bullet + H_2O$ by 11.3 kcal/mol. This considerable energy variance is attributed to structural differences in their respective Jahn–Teller axis configurations (Figure S6). In the $S_2^n cY_Z^\bullet + H_2O$ state, the Jahn–Teller axis of $Mn4^{III}$ is oriented along the D170-Mn4-E333 axis. Contrastingly, in the $S_2^n oY_Z^\bullet + H_2O$ state, Mn1 now $Mn^{III}$, aligns its Jahn–Teller axis along the O3−Mn1-E189 axis. This geometrical alteration results in a significantly destabilized bond between $\mu$-oxo and $Mn1^{III}$, with a length of 2.39 Å accounting for the substantial energy difference between the $S_2^n cY_Z^\bullet + H_2O$ and $S_2^n oY_Z^\bullet + H_2O$. Notably, the alternative Jahn–Teller axis features the detachment of E189 from Mn1 (Figure S7), as observed by Ibrahim et al. in their 150 and 250 $\mu$s 2F XFEL structures.[35]

Beyond Jahn–Teller axis configurations, another structural difference between $S_2^n oY_Z^\bullet + H_2O$ and $S_2^n cY_Z^\bullet + H_2O$ lies in their respective hydrogen bond networks. $S_2^n oY_Z^\bullet + H_2O$ retains most of the hydrogen bonds from $S_2^n cY_Z^\bullet$ and $S_2^n oY_Z^\bullet$, except for those involving W2 due to changes in its protonation state. However, the introduction of water to $S_2^n cY_Z^\bullet$ induces a significant alteration in the hydrogen bond network. In the $S_2^n cY_Z^\bullet$ state, W1 donates hydrogen bonds to the S169 backbone and D61 when Mn4 is 5-coordinated. In $S_2^n cY_Z^\bullet + H_2O$, the addition of an extra ligand to Mn4 prompts a slight rotation of W2 and W1 to accommodate O6. This reorientation disrupts the existing hydrogen bond between W1 and the backbone oxygen of S169, leading W1 to form a new hydrogen bond with WN1 (Figures 3A and S8). As a consequence, unlike WN1 in $S_2^n cY_Z^\bullet$, $S_2^n oY_Z^\bullet$, and $S_2^n oY_Z^\bullet + H_2O$—which accepts two hydrogen bonds from R357 and the side chain hydroxyl of S169 (S169OH)—the WN1 in $S_2^n cY_Z^\bullet + H_2O$ accepts three hydrogen bonds, receiving the third one from W1. This third hydrogen bond, W1 → WN1, unique to the closed-cubane structure in the $S_2^n Y_Z^\bullet + H_2O$ state, emerges only when a sixth ligand is introduced to Mn4.

Our calculations comparing the wild type (WT) and the S169A mutant provide additional evidence on the closed-cubane state as the more favorable state for WI, corroborating experimental observations. Experimentally, when S169 is mutated to alanine, the PSII core complexes exhibit a ∼ 2.7-fold slower rate of decay from $S_2 \to S_1$ compared to the wild-type, as measured polarographically.[74] Furthermore, unlike the WT where Mn4 binds ammonia at the $S_2$ state, the EPR signal of the $S_2$ state in the S169A mutant remains unaffected by ammonia treatment.[74] This observation suggests that Mn4 in the OEC of the $S_2$ state of S169A is six-coordinated, indicating an early binding of water ligand to the OEC during the $S_1 \to S_2$ transition,[75] which accounts for the slower decay rate from $S_2$ to the $S_1$. To validate such early binding of water in S169A, we optimized structures for both WT and S169A at the $S_1^n Y_Z$ state and a hypothesized $S_2^+ Y_Z + H_2O$ state, where an additional water is inserted to the $S_2^+ Y_Z$ state (Figure 3B). For each state, the hydrogen bond network of lowest energy, to the best of our knowledge, is chosen to represent the states (Figure S3). Our computational analysis shows that this early water binding is feasible in the closed-cubane form of $S_2^+ Y_Z$ and is energetically more favorable for S169A than for WT, with the $\Delta G(S_1^n Y_Z \to S_2^+ Y_Z + H_2O)$ for S169A lower by 4.0 kcal/mol compared to WT. Therefore, our calculations validate the early binding of

**Figure 3.** Evidence that a closed-cubane is more favorable for WI. (A) Comparison of the closed- and open-cubane conformers at the $S_2Y_Z^\bullet$ states. $S_2^noY_Z^\bullet$ is energetically more favorable than $S_2^ncY_Z^\bullet$ by 3.0 kcal/mol. In contrast, $S_2^noY_Z^\bullet+H_2O$ is less favorable by 11.3 kcal/mol compared to $S_2^ncY_Z^\bullet+H_2O$. As a result, $\Delta G(S_2^noY_Z^\bullet, WI)$ is 14.3 kcal/mol higher than $\Delta G(S_2^ncY_Z^\bullet, WI)$, making $S_2^ncY_Z^\bullet$ a better candidate for WI. The difference between the hydrogen bond networks of $S_2^ncY_Z^\bullet+H_2O$ and $S_2^noY_Z^\bullet+H_2O$ is highlighted, with W1 donating a hydrogen bond to the backbone O of S169 in $S_2^noY_Z^\bullet+H_2O$ and to WN1 in $S_2^ncY_Z^\bullet+H_2O$. (B) Early binding of water to the S169A mutant during the $S_1 \rightarrow S_2$ transition, facilitated by W1 shifting its hydrogen bond acceptor. When inserting the water to the closed-cubane form of $S_2^nY_Z$, the $\Delta G(S_1^nY_Z \rightarrow S_2^+Y_Z+H_2O)$ for S169A is lower by 4.0 kcal/mol compared to WT. This energy difference can be accounted for by a change in the hydrogen bond network: mutating S169 to alanine eliminates the S169OH $\rightarrow$ WN1 hydrogen bond, making the W1 $\rightarrow$ WN1 hydrogen bond more favorable. Since the W1 $\rightarrow$ WN1 hydrogen bond only occurs in the presence of an extra ligand binding to Mn4 in the closed-cubane state, the propensity for water binding to the S169A mutant with the W1 $\rightarrow$ WN1 hydrogen bond is increased.
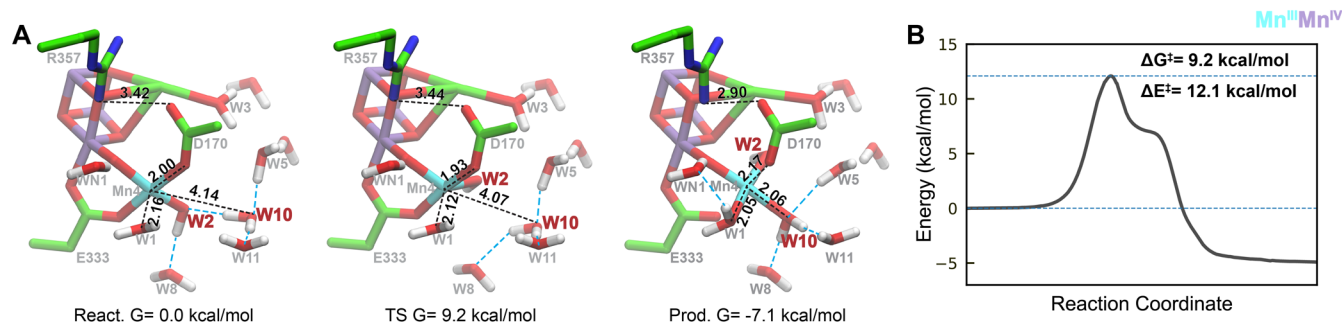


**Figure 4.** WI of W2 at $S_2^ncY_Z^\bullet$ described by QM/MM. (A) The process is characterized by the rotation of W2 ($OH^-$) to be the O6 of the OEC, forming a hydrogen bond with O5 and the spontaneous binding of W10 to $Mn4^{III}$. (B) Energy of the cluster along the IRC path, which exhibits a free energy barrier of 9.2 kcal/mol and an energy barrier of 12.1 kcal/mol.

water in the $S_2$ state of S169A and reinforce the assertion that WI preferentially occurs in the closed-cubane state.

This early binding of water in the S169A mutant is facilitated by a change in the hydrogen bond network that exists only in the closed-cubane form (Figure 3B). In both the $S_1^nY_Z$ and the hypothetical $S_2^+Y_Z+H_2O$ states, WT and S169A exhibit similar hydrogen bond networks, with the key distinction being the absence of the hydrogen bond between the S169OH and WN1 in the S169A mutant. Consequently, WN1 in S169A seeks an alternative hydrogen bond donor to compensate, with W1 being a suitable candidate. Therefore, in the optimized structure of $S_2^+Y_Z+H_2O$, W1 shifts its hydrogen bond from the backbone of residue 169 to WN1. This shift is analogous to

the changes observed in $S_2^ncY_Z^\bullet+H_2O$ (Figure 3A), where the introduction of an additional ligand to Mn4 in the closed-cubane structure induces a slight rotation in W2 and W1 to accommodate this ligand. This rotation reorients the Mn4–W1 axis and breaks the hydrogen bond between W1 and the backbone oxygen of residue 169, forming a new hydrogen bond between W1 and WN1 (Figure S8). In contrast, in the $S_1^nY_Z$ state, where no extra ligand alters the Mn4–W1 axis, W1 retains its hydrogen bond to the backbone of residue 169. As a result, mutating S169 to alanine eliminates the S169OH $\rightarrow$ WN1 hydrogen bond, making the W1 $\rightarrow$ WN1 hydrogen bond more favorable. Since the W1 $\rightarrow$ WN1 hydrogen bond occurs only in the presence of an extra ligand binding to Mn4 in the
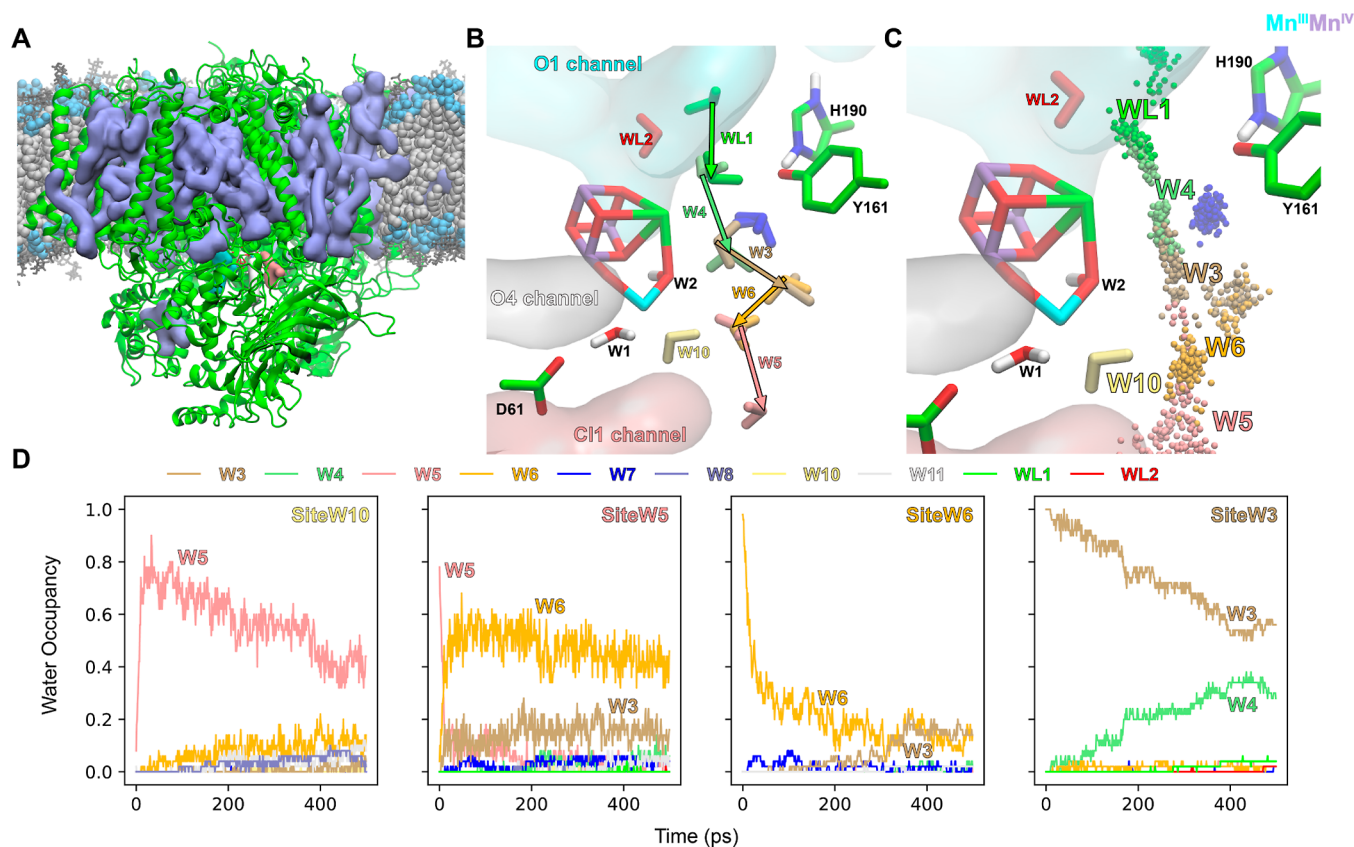
**Figure 5.** Replenishment of W10 after its binding to Mn4 depicted by molecular dynamics (MD). (A) All-atom MD system of the PSII monomer, featuring three water channels that originate from the OEC in a *T. vulcanus* membrane. Protein is rendered in green with cartoon representation. Lipids and pigments solved by X-ray structures are in perano blue with surface representation. Head groups of the lipid bilayer are in sky blue and the lipid tails are in silver with vDW representation. Glycans of the lipid bilayer are in gray with licorice representation. (B) Representative MD replica, out of 50, depicting the water flowing into the original site of W10 (SiteW10). Colored licorice waters represent the state before (0 ps) and after (153 ps) water inflow and arrows indicate the direction of water flow. History of the oxygen positions is indicated by small points in (C). (D) Water occupancy at various sites over time. The occupancy of a specific water molecule at a given water site at time t is calculated as the number of replicas in which this particular water molecule is present at the designated site at time t, divided by the total number of replicas.

closed-cubane state, the propensity for water binding to the S169A mutant with the W1 → WN1 hydrogen bond is increased. This heightened inclination for water binding in the S169A mutant underscores the suitability of the closed-cubane state for WI, aligning the computational predictions with the experimental findings.

**Dynamics of the Water Insertion during the $S_2 \rightarrow S_3$ Transition.** With $S_2^n cY_Z^\bullet$ being a better candidate for WI, we choose to add a water to it. We employ a strategy where we assign W2 as an OH⁻, serving as an example of the water inserted into the OEC. Following this strategy, we searched for the transition state of rotating W2 into the O6 position, forming a hydrogen bond with O5. In the resulting IRC, we observed that W10 spontaneously occupies the original position of W2, stabilizing the system by 7.1 kcal/mol (Figure 4A).

For such a rotation of W2 accompanied by the binding of W10 to Mn4, our transition state search and IRC calculations indicate an energy barrier of 12.1 kcal/mol and a free energy barrier of 9.2 kcal/mol (Figure 4B). The transition state captures the moment where W2 has undergone partial rotation, and Mn4 maintains its original five ligands. After the transition state, W10 binds to Mn4, compensating for the energy required for the rotation. Such incorporation of W10 involves breaking a hydrogen bond between W2 and W8 and

forming a hydrogen bond between W10 and W8. Notably, the hydrogen bond acceptor of W1 shifts from the backbone of S169 to WN1, as observed in the structural difference between $S_2^n cY_Z^\bullet$ and $S_2^n cY_Z^\bullet + H_2O$ (Figure S8). In addition, the transition state reflects a change in the Jahn–Teller axis orientation: before the WI, Mn4 possesses five ligands with the Jahn–Teller axis oriented along the W1–Mn4 bond at $S_2 cY_Z^\bullet$. After the WI, the Jahn–Teller axis reorients to align with the D170-Mn4-E333 axis. The new Jahn–Teller axis diminishes the interaction between D170 and Mn4. This weaker interaction results in D170 forming a stronger electrostatic interaction with R357, contributing to the −7.1 kcal/mol stabilization energy.

Due to the limitations of the IRC method, which does not account for thermal fluctuations, our product of WI is trapped at a local minimum where the original site of W10 remains vacant. Ideally, we would observe the spontaneous movement of dynamic water molecules to fill this site. To capture the dynamics of the replenishment of W10 after it binds to Mn4, we initiated MD simulations, beginning with the coordinates of the QM/MM IRC-derived product (Figure 5). We constructed an all-atom MD system of a *Thermosynechococcus vulcanus* PSII monomer from PDB entries 3WU2, 4V62, and 4UB6, incorporating its native membrane bilayer (Figure 5A). The system is carefully equilibrated (see Method in Supporting
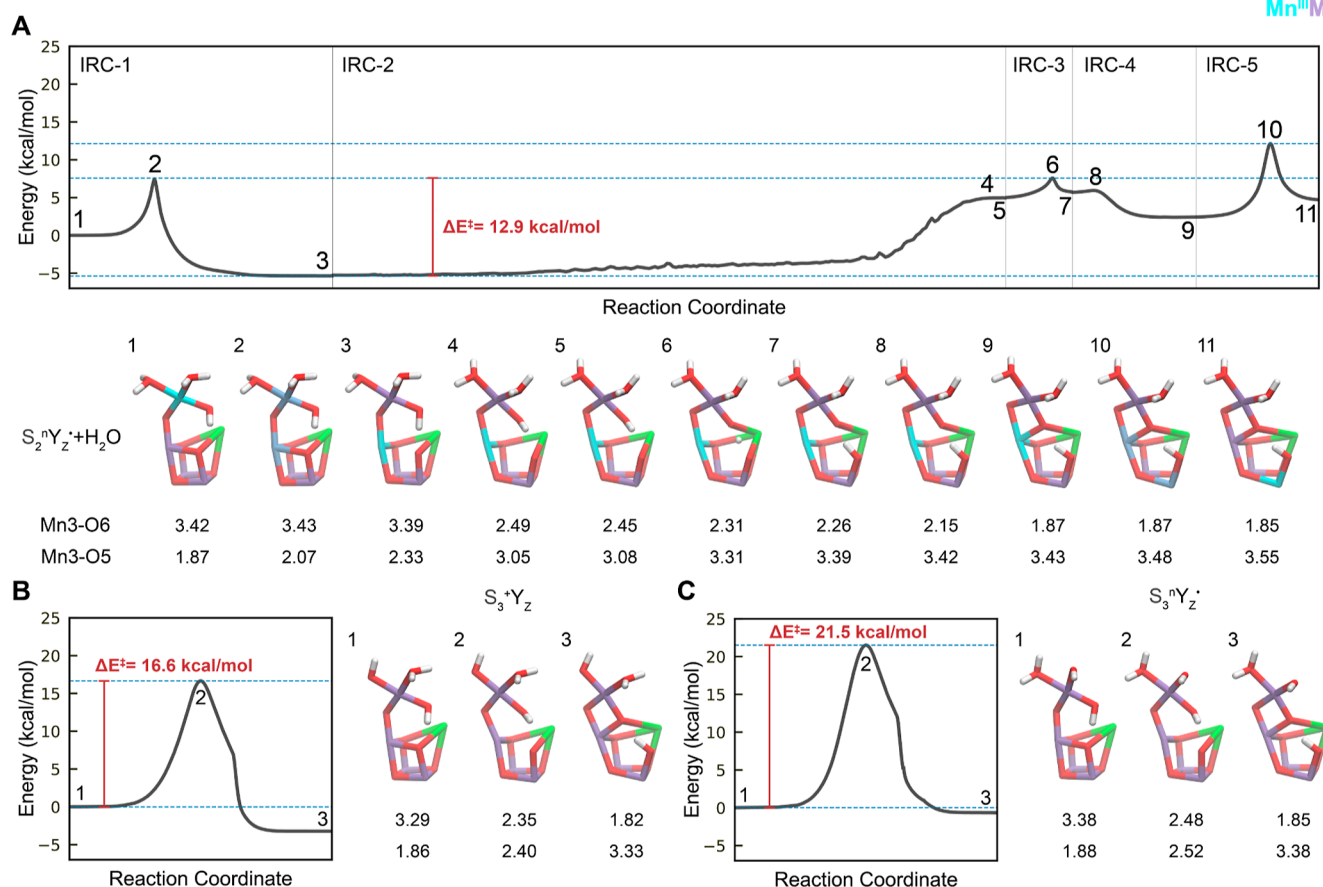
**Figure 6.** Closed-cubane to open-cubane isomerization resulting from the ligand exchange of Mn3 between O5 and O6 post WI. (A) Five steps are characterized to isomerize from $S_2^n cY_Z^\bullet + H_2O$ to $S_2^n oY_Z^\bullet + H_2O$: (1) electron transfer from Mn4$^{III}$ to Mn3$^{IV}$, forming a 4434-closed-cubane state (1−2−3, IRC-1). (2) Ligand exchange at Mn3$^{III}$, leading to the closed-cubane to open-cubane isomerization (3−4−5, IRC-2). (3) Proton transfer from O6 to O5 (5−6−7, IRC-3). (4) Jahn−Teller axis change of Mn3$^{III}$, from the O5/O6−Mn3-E354 axis to the O3−Mn3−O4 axis (7−8−9, IRC-4). (5) Electron transfer from Mn3$^{III}$ to Mn1$^{IV}$ (9−10−11, IRC-5). Through the five steps, O6 is brought to Mn3 gradually, while O5 dissociates from Mn3. The isomerizations at (B) $S_3^+ Y_Z$ and (C) $S_3^n Y_Z^\bullet$ exhibit a spontaneous proton transfer as the O5 and O6 ligands of Mn3 exchange, leading to energy barriers of 16.6 and 21.5 kcal/mol, respectively.

Information) to hydrate the three water channels that originated from the OEC (Figure 1C), with the atoms in the QM layer of our QM/MM model restrained.

After the equilibration steps, we released the restraints and executed 50 replicas of 500 ps simulations to monitor the sequential movement of water molecules and the dynamic occupancy of water sites to replenish W10 (Figure 5B,C). The occupancy of a specific water molecule at a given water site (SiteWx) at time t is calculated as the number of replicas in which this particular water molecule is present at the designated site at time t divided by the total number of replicas. Our analysis revealed that in approximately 80% of the replicas, W5 occupies SiteW10 within the initial 35 ps. Concurrently, either W6 or W3 occupy SiteW5 (Figure 5D). The occupancy at SiteW6 accumulates more slowly and never reaches 100% due to the slow migration of W3 to SiteW6 and W4 to SiteW3, which occurs on the time scale of a few nanoseconds (Figure 5D). This vacancy at SiteW6 can be attributed to the slow ligand exchange at Ca$^{2+}$, where W4 migrates to SiteW3 and SiteW4 is subsequently replenished by WL1 from the O1 channel, recently proposed by the XFEL analysis to be the origin of O6.[37] The O1 channel connecting the W4 to the bulk water contains many hydrophobic amino

acids,[80] leading to high water mobility so we ended the occupancy analysis at SiteW4.

Our calculations described above partition the water delivery process into two subprocesses: (1) the rotation of W2 transforms it into O6 characterized by QM/MM with a free energy barrier of 9.2 kcal/mol, which suggests a spontaneous binding of W10. (2) the replenishment of W10 is characterized by MD simulations on a time scale of hundreds of picoseconds, which involve a sequential movement of W5, W6, W3, and W4 to replenish SiteW10. Considering the fact that water replenishment happens within a few nanoseconds, the free energy barrier should be substantially low enough to be overcome by small thermal fluctuations. Therefore, the second subprocess may occur before the first has fully been completed, supporting the notion that the rotation of W2 with binding of W10 to Mn and the replenishment of W10 are concerted. In addition, we are not limiting W10 as the only possible water molecule that binds to Mn4, due to a lack of thermal fluctuations in QM/MM calculations. It is possible that the IRC follows this path because the hydrogen bond network is well maintained, resulting in a favorable local minimum. Given more thermal fluctuations, it is possible that other water molecules in the chain leading from the O1 channel have a chance to bind Mn4 directly. In summary, we hereby propose a

Ca-carousel mechanism where a $OH^-$ rotates to the closed-cubane and becomes O6, and its replenishment in a concerted operation requires a sequential movement of water molecules via a ligand exchange at $Ca^{2+}$. In our study, we used W2 as a representative $OH^-$ for insertion, but it is worth noting that other water molecules like W3 could potentially serve the same role.[29,48,68,69,72]

**Open-Cubane and Closed-Cubane Isomerization Post Water Insertion.** After the WI leading to the $S_2^n Y_Z{}^\bullet + H_2O$ state, the OEC advances toward O–O bond formation. By transferring an electron to $Y_Z{}^\bullet$ to transition to the $S_3^+ Y_Z$ state and subsequently releasing a proton to achieve the $S_3^n Y_Z{}^\bullet$ state, the OEC reaches the final stable state prior to O–O bond formation. Intriguingly, similar to the fact that the $S_2^n Y_Z{}^\bullet + H_2O$ state can adopt both the open- and closed-cubane configurations, computational models have postulated analogous isomeric forms for the $S_3^+ Y_Z$ and $S_3^n Y_Z{}^\bullet$ states.[56] However, the exact conformation, whether open- or closed-cubane that sets the stage for O–O bond formation remains under discussion. To delve deeper into this question, we conducted QM/MM calculations to characterize the isomerization from a closed-cubane to an open-cubane structure, seeking insights into the state that ultimately precedes O–O bond formation. To simplify the computations, all unpaired electrons were set to the alpha spin state for transition state searches and IRC calculations. We investigated the isomerization of closed-cubane to open-cubane conformers at 3 states: $S_2^n Y_Z{}^\bullet + H_2O$, $S_3^+ Y_Z$, and $S_3^n Y_Z{}^\bullet$. All three isomerizations involve a ligand exchange at Mn3 between O5 and O6, accompanied by a proton transfer that swaps the positions of $\mu$-oxo and a $OH^-$. Consequently, O5, which begins as a $\mu$-oxo, transforms into a $OH^-$ disengaged from Mn3, while O6, initially a $OH^-$, becomes a $\mu$-oxo coordinated to Mn3 (Figure 6).

For the isomerization at $S_2^n Y_Z{}^\bullet + H_2O$ (Figure 6A), we characterized four intermediate states (A3, A5, A7, and A9) transitioning from $S_2^n c Y_Z{}^\bullet + H_2O$ (A1) to $S_2^n o Y_Z{}^\bullet + H_2O$ (A11). These intermediate states are interconnected through a sequence of five IRC calculations involving five transition states (A2, A4, A6, A8, and A10). The five IRC calculations present energy barriers of 7.1 10.3, 2.6, 0.3, and 9.7 kcal/mol, respectively.

Initially, we identified an electron transfer from $Mn4^{III}$ to $Mn3^{IV}$ for the O5 and the O6 to exchange. The electron transfer via state A2 produces a 4434-closed-cubane state (state A3), where O6 moves slightly closer to Mn3, from 3.42 to 3.39 Å, and O5 moves away from Mn3, from 1.87 to 2.33 Å. The change of Mn Mulliken spin population (Figure S9A) further evidences the electron transfer from $Mn4^{III}$ to $Mn3^{IV}$, leading to a shift of the Jahn–Teller axis of $Mn^{III}$ from the D170-Mn4-E333 axis to the O5/O6–Mn3-E354 axis (Figure S10). This reorientation in the Jahn–Teller axis maximizes flexibility for the subsequent ligand exchange between O5 and O6 (IRC-2), resulting in the most significant changes in the binding of O6 to Mn3 and the binding of the O5 to the Mn3 bond length (Figure S10A). During this step, the length of the Mn3–O6 bond decreases to 2.49 from 3.39 Å, while that of the Mn3–O5 bond moves further away to 3.08 from 2.33 Å, culminating in O6 being a $OH^-$ ligated to Mn3 in state A5. A subsequent proton transfer (IRC-3) brings O6 even closer to Mn3 (2.26 Å) and moves O5 further away (3.39 Å), resulting in a 4434-open-cubane configuration (state A7). Cumulatively, the transition from closed-cubane (state A3) to open-cubane (state A7) presents an overall energy barrier of 12.9 kcal/mol.

Notably, during the transition from the closed-cubane to the open-cubane, the hydrogen bond acceptor of W1 shifts from the backbone of S169 to WN1, reaffirming that the W1 → WN1 hydrogen bond occurs only in the presence of an extra ligand binding to Mn4 in the closed-cubane state (Figures 3 and S8).

The state A7 can either proceed to $S_3^+ o Y_Z$ via an electron transfer from $Mn3^{III}$ to $Y_Z{}^\bullet$, or isomerize to state A9 through A8. The latter isomerization reorients the Jahn–Teller axis from the O5/O6–Mn3-E354 axis to the O4–Mn3–O3 axis, resulting in Mn3–O6 and Mn3–O5 distances of 1.87 and 3.43 Å, respectively. Lastly, an electron transfer from $Mn3^{III}$ to $Mn1^{IV}$ finalizes the $S_2^n o Y_Z{}^\bullet + H_2O$ state, with Mn3–O6 and Mn3–O5 distances settling at 1.85 and 3.55 Å. In our calculations, the electron transfer from $Mn3^{III}$ to $Mn1^{IV}$ is preceded by a transition to state A9, a Jahn–Teller axis isomer of A7, resulting in a relatively high energy barrier from A9 to A11. Given the inherent complexities of the reaction, where numerous bond lengths change, our strategy of segmenting the process might have overcomplicated this electron transfer. Since we cannot exhaustively scan all bond changes, it is plausible that alternative pathways with potentially more favorable energy barriers could exist. In summary, the isomerization at $S_2^n Y_Z{}^\bullet + H_2O$ starts from $S_2^n c Y_Z{}^\bullet + H_2O$ and undergoes an electron transfer from $Mn4^{III}$ to $Mn3^{IV}$, which provides the flexibility for O6 and O5 to exchange, followed by the proton transfer from O6 to O5. Subsequently, another electron transfer from $Mn3^{III}$ to $Mn1^{IV}$ concludes the isomerization, resulting in the $S_2^n o Y_Z{}^\bullet + H_2O$ state.

We further characterized some of the intermediate states at varying spin states (Tables S7 and S8), including $\alpha\alpha\alpha\beta\alpha$, $\alpha\beta\alpha\alpha$, and $\alpha\beta\alpha\beta\alpha$. The energy differences among these configurations were within $\pm 1.6$ kcal/mol relative to the $\alpha\alpha\alpha\alpha\alpha$ state. In addition, since 4434-closed-cubane state (state A3) is surprisingly stable, we characterized it further with the proton hyperfine coupling constants (Supporting Information 1). However, we note that isomerization to state A3 will be competing with state A1 undergoing PCET. The barriers for these two reactions are indistinguishable in our calculations, so both processes should be possible.

For the isomerization at $S_3^+ Y_Z$ (Figure 6B) and $S_3^n Y_Z{}^\bullet$ (Figure 6C), our IRC calculations indicate a spontaneous proton transfer during the ligand exchange between O5 and O6 on Mn3. The transition state of $S_3^+ Y_Z$ (state B2) captures a Mn3–O6 distance of 2.35 Å and a Mn3–O5 distance of 2.40 Å, with O6 retaining the proton until it reaches a Mn3–O6 distance of 1.98 Å (Figure S9B). Similarly, in the transition state for $S_3^n Y_Z{}^\bullet$ (state C2), the Mn3–O6 and Mn3–O5 distances are 2.48 and 2.52 Å, respectively, and O6 holds onto the proton until a Mn3–O6 distance of 2.01 Å (Figure S9C). The energy barriers for these isomerizations are 16.6 kcal/mol for $S_3^+ Y_Z$ and 21.5 kcal/mol for $S_3^n Y_Z{}^\bullet$. Both barriers exceed those of the closed-cubane to open-cubane transition at the $S_2^n Y_Z{}^\bullet + H_2O$ state, likely because $Mn3^{IV}$ provides less flexibility for ligand exchange.

## ■ DISCUSSION

In our exploration of the $S_2 \rightarrow S_3$ transition in PSII, we considered two alternative pathways: one involving WI before PCET and another where PCET precedes WI (Figure 2), while considering both the open- and closed-cubane structures. For the PCET-first pathway, we obtained a stable intermediate state, $S_3^+ c Y_Z - H_2O$, for the closed-cubane, while no local

minimum was found for the corresponding open-cubane state. This difference indicates that the pre-WI PCET is more favorable for the $S_2^n cY_Z^\bullet$ than the $S_2^n oY_Z^\bullet$, which aligns with Pantazis' five-coordinate $S_3$ model,[30] suggesting the pre-WI PCET only occurs to $S_2^n cY_Z^\bullet$. Importantly, we introduced a WI-first pathway, where we inserted a water first and introduced the $S_2^n Y_Z^\bullet + H_2O$ state. The free energy difference for the pre-WI and post-WI PCET concluded that initiating the process with WI results in a 6.6 kcal/mol reduction in the free energy change for the PCET. This reduction underlines the key regulatory role of water binding to the OEC on the redox leveling mechanism of the catalytic cycle. Such redox leveling has originally been discussed in terms of alternating deprotonation of water ligands and oxidation of the OEC.[8,42,70] Here, we find that labile ligand coordination and dissociation are crucial mechanisms adjusting OEC redox behavior.

Additionally, we characterized the transition state of the post-WI PCET, presenting a concerted process of the Mn4-D170OD1 and Mn4-E333OE1 distance shortening and proton relocating. Such a concerted process results in a free energy barrier of 7.6 kcal/mol, which can be overcome within the time scale of 300 $\mu$s for the $S_2 \rightarrow S_3$ transition characterized by time-resolved photothermal beam deflection,[70] thereby further validating our model. From these QM/MM calculations, the reduction principle on Mn can be generalized to inspire the design of other Mn catalysts: The reduction potential of Mn is highly dependent on its ligand environment, which can be lowered by a preinserted ligand like water.

We further delved into the mechanisms of WI using a combination of QM/MM and MD simulations. With QM/MM, we generate closed and open conformations suitable for WI, $S_2^n cY_Z^\bullet + H_2O$ and $S_2^n oY_Z^\bullet + H_2O$. The closed and open OEC conformations exhibit a significant energy difference of 11.3 kcal/mol, primarily due to the location of the $Mn^{III}$ center in the OEC and the orientation of its Jahn−Teller axis. We find that the closed-cubation state is thermodynamically favored for WI (Figure 3A). With transition state search, IRC and MD, we propose a Ca-carousel mechanism where an $OH^-$ rotates to the closed-cubane and becomes O6, replenished through a ligand exchange at $Ca^{2+}$ in a concerted manner (Figures 4 and 5). We used W2 as a representative case, which showed an estimated free energy barrier of 9.2 kcal/mol. The fact that this barrier for WI is lower than the pre-WI PCET ($\Delta G$(pre-WI, PCET) = 12.6 kcal/mol) confirms that the $S_2^n cY_Z^\bullet$ is more likely to incorporate a WI first and then a PCET reaction, the WI-first pathway. Notably, our calculations focus on W2 as a working example and do not exclude the possibility that W3 could also be deprotonated and rotated to become the first O6. Further calculations comparing the energy barriers associated with inserting W2 and W3 are required to draw a definitive conclusion about the exact water substrate.

Our Ca-carousel mechanism not only exhibits an energetically favorable pathway but also provides reasonable interpretations of experimental observations. With the WI studied extensively by experiments, some results in seemingly contradicting mechanisms. For example, the XFEL structures indicate that the O1 channel is the water delivery channel with a high mobility of water during the $S_2 \rightarrow S_3$ transition. However, the studies on the S169A mutation suggest that without S169 anchoring WN1, the $S_2$ state shows early binding of water, indicating the O4 channel is the water delivery channel. Although the two experiments seemingly lead to contradictory conclusions, our calculations rationalize both of them: on the one hand, our results indicate the ligand exchange at $Ca^{2+}$ plays a crucial role in the substrate water delivery, which aligns with the increased water mobility in the O1 channel[36] and water movement around $Ca^{2+}$[37] during the $S_2 \rightarrow S_3$ transition. On the other hand, our model offers an explanation for the proposed early binding of water in the S169A $S_2$ state (Figure 3B).[74,75] Contrary to the notion that the S169A mutation results in a loss of anchoring of the water substrate in the O4 channel for insertion, we propose that the mutation disrupts a hydrogen bond between S169OH and WN1. This disruption, in turn, prompts W1 to reorient toward WN1, which will lead to a relative rotation of W1 and W2 that occurs only in our $S_2^n cY_Z^\bullet + H_2O$ structure. Therefore, such rotation caused by the S169A mutation will prefer ligand binding at the O6 position, which should result in an early binding of water, as proposed on the basis of EPR and DFT QM/MM. In summary, while studies on S169A seemingly indicate that substrate water is delivered from the O4 channel and the XFEL data suggest the O1 channel, our mechanism reconciles the discrepancies between them.

When analyzing our $S_2^n Y_Z^\bullet + H_2O$ structures, we noticed that E189 is not ligated to Mn1 in the $S_2^n oY_Z^\bullet + H_2O$ state. Such unbinding is observed in the 2F XFEL structures, from which a mechanism of inserting water to the open-cubane structure is proposed.[35] However, the mechanism we proposed involving WI into the closed-cubane state, represented by $S_2^n cY_Z^\bullet + H_2O$, does not necessarily conflict with the XFEL findings. Several factors may contribute to the absence of closed-cubane structures in the XFEL studies: first, it is important to note that all XFEL studies use exclusively crystals of cyanobacterial PSII, which does not naturally produce the a $g = 4.1$ signal associated with the closed-cubane structure.[81,82] This specificity might exclude the observation of closed-cubane structures that could be adopted for WI in other species, since we find that it is energetically plausible. Second, the proximity of oxygen atoms to the high and widely distributed electron density of manganese ions makes it challenging to resolve these lighter atoms clearly in XFEL images,[83] potentially obscuring the distinction between closed- and open-cubane states when they are mostly different in oxygen atom positions. Lastly, current XFEL crystallography cannot resolve heterogeneous compositions within the sample,[63,64] so transient intermediates like the proposed closed-cubane structures, which may exist briefly during the transition process, are likely overlooked.

Given the debate over whether the open-cubane or closed-cubane configuration leads to O−O bond formation, especially in species other than cyanobacteria, we investigated the potential isomerization of our proposed closed-cubane state to the open-cubane state after WI. We identified a plausible pathway for isomerization from $S_2^n cY_Z^\bullet + H_2O$ to $S_2^n oY_Z^\bullet + H_2O$ involving a series of intermediates. Within these intermediates, an electron initially on $Mn4^{III}$ transfers to $Mn3^{IV}$, resulting in the change of the Jahn−Teller axis that provides the flexibility for O5 and O6 to exchange, and finally localizes at Mn1. When we consider this multistep isomerization, each step of it competes with the PCET reaction to $S_3^+ Y_Z$—any intermediates along the isomerization path has a chance to proceed to $S_3^+ Y_Z$. In our current study, the first barrier for this isomerization ($S_2^n cY_Z^\bullet + H_2O$ to 4434-closed-cubane) presents a similar barrier to the PCET ($S_2^n cY_Z^\bullet + H_2O$ to $S_3^+ cY_Z$), so that it is beyond the scope of this study to draw a conclusion on whether the OEC isomerizes to the open-cubane at this step.

More calculations of higher accuracy on the PCET reactions starting from states A1, A3, A5, A7, A9, and A11 to their corresponding $S_3^+cY_Z$ or $S_3^+oY_Z$ are required to provide a more detailed picture.

The cubane transformation for $S_2^nY_Z^\bullet + H_2O$ exhibits a barrier of 12.9 kcal/mol, which is significantly lower than the barriers at $S_3^+Y_Z$ and $S_3^nY_Z^\bullet$—16.1 and 21.5 kcal/mol, respectively. We attribute this relatively low barrier compared to $S_3^+Y_Z$ and $S_3^nY_Z^\bullet$ to the flexibility provided by $Mn3^{III}$, which allows for O5 and O6 to exchange. Yet, $S_3$ states lack this flexibility due to $Mn^{IV}$ occupying all sites, resulting in barriers that appear too high for the observed transition time scales of hundreds of $\mu$s. Therefore, we conclude that $S_2^nY_Z^\bullet + H_2O$ is the only possible state for the closed-cubane to isomerize to the open-cubane.

It is important to note that our barrier of 16.1 and 21.5 kcal/mol for isomerization at $S_3^+Y_Z$ and $S_3^nY_Z^\bullet$ is significantly different from the 24.7 and the 14.9 kcal/mol reported by Guo et al., respectively.[56] We attribute these differences to the different definitions of the $S_3$ states. In their structures, the W1 in both $S_3^+Y_Z$ and $S_3^nY_Z^\bullet$ is a $OH^-$, while it is a $H_2O$ sharing a proton with D61 in our structures. Therefore, our model presents an additional proton through the entire Kok Cycle, with the protonation states assigned according to the hyperfine coupling constants from EPR at the $S_2$ state.[42] However, when Guo et al. calculated the barrier for their $S_3^nY_Z^\bullet(W1 = H_2O)$ state, which corresponds to our $S_3^nY_Z^\bullet$, they arrived at a barrier of 23.7 kcal/mol—consistent with our 21.5 kcal/mol, underscoring the impact of protonation states on the isomerization process.

## CONCLUSIONS

In conclusion, our study underscores the critical role played by WI in facilitating the effective oxidation of $Mn^{III}$ by $Y_Z^\bullet$, akin to the primary oxidant in synthetic water-oxidation catalysts. Our findings highlight a general principle: the redox behavior of Mn is significantly influenced by its surrounding ligand environment, which controls the insertion of water ligands to enhance reactivity. Combining QM/MM and MD simulations, we propose a Ca-carousel mechanism for the delivery of water to the closed form of the OEC through ligand exchange at $Ca^{2+}$. This mechanism establishes a key role of the closed-cubane form of the OEC and reconciles experimental observations from S169A mutations and XFEL data. Furthermore, we characterize the isomerization from closed- to open-cubane conformations after WI, and we demonstrate the convertibility through the location of $Mn^{III}$ and the orientation of its Jahn−Teller axis. In summary, our study not only clarifies the intrinsic interplay between Mn and its ligand environment essential for activation of the OEC but also provides valuable principles for designing Mn-based catalysts in synthetic applications.

## ASSOCIATED CONTENT

### Supporting Information

The Supporting Information is available free of charge at https://pubs.acs.org/doi/10.1021/jacs.4c02926.

> Computation details of QM/MM calculations and MD simulations; $S_2^+Y_Z$ states of different protonation states and hydrogen bond networks; simulated EXAFS of the $S_3^+Y_Z$ states; structural details and energetics of possible states during the $S_2 \rightarrow S_3$ transition; numbering of water molecules; energetics of possible states during the $S_2 \rightarrow$ $S_3$ transition at varying spin states; and magnetic structure and proton hyperfine coupling constants for state A3 in Figure 6A (PDF)

> PCET reaction in Figure 2B (MP4)

> WI reaction in Figure 4 (MP4)

> Replenishment of water in Figure 5B (MP4)

> Isomerization from $S_2^ncY_Z^\bullet + H_2O$ to $S_2^noY_Z^\bullet + H_2O$ in Figure 6A (MP4)

> Isomerization from $S_3^+cY_Z$ to $S_3^+oY_Z$ in Figure 6B (MP4)

> Isomerization from $S_3^ncY_Z^\bullet$ to $S_3^noY_Z^\bullet$ in Figure 6C (MP4)

## AUTHOR INFORMATION

### Corresponding Author

**Victor S. Batista** − *Department of Chemistry, Yale University, New Haven, Connecticut 06520, United States;* orcid.org/0000-0002-3262-1237; Email: victor.batista@yale.edu

### Authors

**Jinchan Liu** − *Department of Molecular Biophysics and Biochemistry, Yale University, New Haven, Connecticut 06520, United States;* orcid.org/0000-0003-2217-1233

**Ke R. Yang** − *Key Laboratory of Advanced Energy Materials Chemistry (Ministry of Education), College of Chemistry, Nankai University, Tianjin 300071, China*

**Zhuoran Long** − *Department of Chemistry, Yale University, New Haven, Connecticut 06520, United States;* orcid.org/0000-0002-2957-9568

**William H. Armstrong** − *Department of Chemistry, Boston College, Chestnut Hill, Massachusetts 02467, United States*

**Gary W. Brudvig** − *Department of Molecular Biophysics and Biochemistry, Yale University, New Haven, Connecticut 06520, United States; Department of Chemistry, Yale University, New Haven, Connecticut 06520, United States;* orcid.org/0000-0002-7040-1892

Complete contact information is available at:
https://pubs.acs.org/10.1021/jacs.4c02926

### Notes

The authors declare no competing financial interest.

## REFERENCES

(1) Nelson, N.; Yocum, C. F. Structure and function of photosystem I and II. *Annu. Rev. Plant Biol.* **2006**, *57*, 521−565.

(2) McEvoy, J. P.; Brudvig, G. W. Water-splitting chemistry of photosystem II. *Chem. Rev.* **2006**, *106*, 4455−4483.

(3) Shen, J. R. The Structure of Photosystem II and the Mechanism of Water Oxidation in Photosynthesis. *Annu. Rev. Plant Biol.* **2015**, *66*, 23−48.

(4) Umena, Y.; Kawakami, K.; Shen, J. R.; Kamiya, N. Crystal structure of oxygen-evolving photosystem II at a resolution of 1.9 Å. *Nature* **2011**, *473*, 55−60.

(5) Cox, N.; Pantazis, D. A.; Lubitz, W. Current Understanding of the Mechanism of Water Oxidation in Photosystem II and Its Relation to XFEL Data. *Annu. Rev. Plant Biol.* **2020**, *89*, 795−820.

(6) Joliot, B.; Barbieri, G.; Chabaud, R. Un nouveau modele des centres photochimiques du systeme II. *Photochem & Photobiology* **1969**, *10*, 309−329.

(7) Kok, B.; Forbush, B.; McGloin, M. Cooperation of charges in photosynthetic O₂ evolution-I. A linear four step mechanism. *Photochem & Photobiology* **1970**, *11*, 457−475.

(8) Klauss, A.; Haumann, M.; Dau, H. Alternating electron and proton transfer steps in photosynthetic water oxidation. *Proc. Natl. Acad. Sci. U.S.A.* **2012**, *109*, 16035−16040.

(9) Bowes, J. M.; Crofts, A. R.; Itoh, S. A high potential acceptor for photosystem II. *Biochim. Biophys. Acta Bioenerg.* **1979**, *547*, 320−335.

(10) Metz, J. G.; Nixon, P. J.; Rogner, M.; Brudvig, G. W.; Diner, B. A. Directed alteration of the D1 polypeptide of photosystem II: evidence that tyrosine-161 is the redox component, Z, connecting the oxygen-evolving complex to the primary electron donor, P680. *Biochemistry* **1989**, *28*, 6960−6969.

(11) Styring, S.; Sjöholm, J.; Mamedov, F. Two tyrosines that changed the world: interfacing the oxidizing power of photochemistry to water splitting in photosystem II. *Biochim. Biophys. Acta Bioenerg.* **2012**, *1817*, 76−87.

(12) Rappaport, F.; Diner, B. A. Primary photochemistry and energetics leading to the oxidation of the $(Mn)_4Ca$ cluster and to the evolution of molecular oxygen in Photosystem II. *Coord. Chem. Rev.* **2008**, *252*, 259−272.

(13) Mandal, M.; Kawashima, K.; Saito, K.; Ishikita, H. Redox Potential of the Oxygen-Evolving Complex in the Electron Transfer Cascade of Photosystem II. *J. Phys. Chem. Lett.* **2020**, *11*, 249−255.

(14) Tamura, H.; Saito, K.; Nishio, S.; Ishikita, H. Electron-Transfer Route in the Early Oxidation States of the $Mn_4CaO_5$ Cluster in Photosystem II. *J. Phys. Chem. B* **2023**, *127*, 205−211.

(15) Dau, H.; Zaharieva, I. Principles, efficiency, and blueprint character of solar-energy conversion in photosynthetic water oxidation. *Acc. Chem. Res.* **2009**, *42*, 1861−1870.

(16) Oliver, T.; Kim, T. D.; Trinugroho, J. P.; Cordón-Preciado, V.; Wijayatilake, N.; Bhatia, A.; Rutherford, A. W.; Cardona, T. The Evolution and Evolvability of Photosystem II. *Annu. Rev. Plant Biol.* **2023**, *74*, 225−257.

(17) Linke, K.; Ho, F. M. Water in photosystem II: structural, functional and mechanistic considerations. *Biochim. Biophys. Acta* **2014**, *1837*, 14−32.

(18) Sakashita, N.; Watanabe, H. C.; Ikeda, T.; Saito, K.; Ishikita, H. Origins of Water Molecules in the Photosystem II Crystal Structure. *Biochemistry* **2017**, *56*, 3049−3057.

(19) Sirohiwal, A.; Pantazis, D. A. Functional water networks in fully hydrated photosystem II. *J. Am. Chem. Soc.* **2022**, *144*, 22035−22050.

(20) Sproviero, E. M.; Gascón, J. A.; McEvoy, J. P.; Brudvig, G. W.; Batista, V. S. Computational studies of the O₂-evolving complex of photosystem II and biomimetic oxomanganese complexes. *Coord. Chem. Rev.* **2008**, *252*, 395−415.

(21) Noguchi, T.; Sugiura, M. Flash-induced FTIR difference spectra of the water oxidizing complex in moderately hydrated photosystem II core films: effect of hydration extent on S-state transitions. *Biochemistry* **2002**, *41*, 2322−2330.

(22) Suzuki, H.; Sugiura, M.; Noguchi, T. Monitoring water reactions during the S-state cycle of the photosynthetic water-oxidizing center: detection of the DOD bending vibrations by means of Fourier transform infrared spectroscopy. *Biochemistry* **2008**, *47*, 11024−11030.

(23) Messinger, J.; Badger, M.; Wydrzynski, T. Detection of one slowly exchanging substrate water molecule in the S₃ state of photosystem II. *Proc. Natl. Acad. Sci. U.S.A.* **1995**, *92*, 3209−3213.

(24) Hillier, W.; Wydrzynski, T. The affinities for the two substrate water binding sites in the O₂ evolving complex of photosystem II vary independently during S-state turnover. *Biochemistry* **2000**, *39*, 4399−4405.

(25) Cox, N.; Messinger, J. Reflections on substrate water and dioxygen formation. *Biochim. Biophys. Acta* **2013**, *1827*, 1020−1030.

(26) Vinyard, D. J.; Brudvig, G. W. Progress toward a molecular mechanism of water oxidation in photosystem II. *Annu. Rev. Phys. Chem.* **2017**, *68*, 101−116.

(27) Chernev, P.; Aydin, A. O.; Messinger, J. On the simulation and interpretation of substrate-water exchange experiments in photosynthetic water oxidation. *Photosynth. Res.* **2024**.

(28) Isobe, H.; Shoji, M.; Shen, J.-R.; Yamaguchi, K. Strong coupling between the hydrogen bonding environment and redox chemistry during the S₂ to S₃ transition in the oxygen-evolving complex of photosystem II. *J. Phys. Chem. B* **2015**, *119*, 13922−13933.

(29) Shoji, M.; Isobe, H.; Yamaguchi, K. QM/MM study of the S₂ to S₃ transition reaction in the oxygen-evolving complex of photosystem II. *Chem. Phys. Lett.* **2015**, *636*, 172−179.

(30) Retegan, M.; Krewald, V.; Mamedov, F.; Neese, F.; Lubitz, W.; Cox, N.; Pantazis, D. A. A five-coordinate Mn(IV) intermediate in biological water oxidation: Spectroscopic signature and a pivot mechanism for water binding. *Chem. Sci.* **2016**, *7*, 72−84.

(31) Capone, M.; Narzi, D.; Bovi, D.; Guidoni, L. Mechanism of water delivery to the active site of photosystem II along the S₂ to S₃ Transition. *J. Phys. Chem. Lett.* **2016**, *7*, 592−596.

(32) Beal, N. J.; Corry, T. A.; O'Malley, P. J. Comparison between Experimental and Broken Symmetry Density Functional Theory (BS-DFT) Calculated Electron Paramagnetic Resonance (EPR) Parameters of the S₂ State of the Oxygen-Evolving Complex of Photosystem II in Its Native (Calcium) and Strontium-Substituted Form. *J. Phys. Chem. B* **2017**, *121*, 11273−11283.

(33) Sakamoto, H.; Shimizu, T.; Nagao, R.; Noguchi, T. Monitoring the Reaction Process During the $S_2 \rightarrow S_3$ Transition in Photosynthetic Water Oxidation Using Time-Resolved Infrared Spectroscopy. *J. Am. Chem. Soc.* **2017**, *139*, 2022−2029.

(34) Saito, K.; Mino, H.; Nishio, S.; Ishikita, H. Protonation structure of the closed-cubane conformation of the O₂-evolving complex in photosystem II. *PNAS Nexus* **2022**, *1*, pgac221.

(35) Ibrahim, M.; Fransson, T.; Chatterjee, R.; Cheah, M. H.; Hussein, R.; Lassalle, L.; Sutherlin, K. D.; Young, I. D.; Fuller, F. D.; Gul, S.; Kim, I. S.; Simon, P. S.; de Lichtenberg, C.; Chernev, P.; Bogacz, I.; Pham, C. C.; Orville, A. M.; Saichek, N.; Northen, T.; Batyuk, A.; Carbajo, S.; Alonso-Mori, R.; Tono, K.; Owada, S.; Bhowmick, A.; Bolotovsky, R.; Mendez, D.; Moriarty, N. W.; Holton, J. M.; Dobbek, H.; Brewster, A. S.; Adams, P. D.; Sauter, N. K.; Bergmann, U.; Zouni, A.; Messinger, J.; Kern, J.; Yachandra, V. K.; Yano, J. Untangling the sequence of events during the $S_2 \rightarrow S_3$ transition in photosystem II and implications for the water oxidation mechanism. *Proc. Natl. Acad. Sci. U.S.A.* **2020**, *117*, 12624−12635.

(36) Hussein, R.; Ibrahim, M.; Bhowmick, A.; Simon, P. S.; Chatterjee, R.; Lassalle, L.; Doyle, M.; Bogacz, I.; Kim, I. S.; Cheah, M. H.; Gul, S.; de Lichtenberg, C.; Chernev, P.; Pham, C. C.; Young, I. D.; Carbajo, S.; Fuller, F. D.; Alonso-Mori, R.; Batyuk, A.; Sutherlin, K. D.; Brewster, A. S.; Bolotovsky, R.; Mendez, D.; Holton, J. M.; Moriarty, N. W.; Adams, P. D.; Bergmann, U.; Sauter, N. K.; Dobbek, H.; Messinger, J.; Zouni, A.; Kern, J.; Yachandra, V. K.; Yano, J. Structural dynamics in the water and proton channels of photosystem II during the S₂ to S₃ transition. *Nat. Commun.* **2021**, *12*, 6531.

(37) Li, H.; Nakajima, Y.; Nango, E.; Owada, S.; Yamada, D.; Hashimoto, K.; Luo, F.; Tanaka, R.; Akita, F.; Kato, K.; Kang, J.; Saitoh, Y.; Kishi, S.; Yu, H.; Matsubara, N.; Fujii, H.; Sugahara, M.; Suzuki, M.; Masuda, T.; Kimura, T.; Thao, T. N.; Yonekura, S.; Yu, L.-J.; Tosha, T.; Tono, K.; Joti, Y.; Hatsui, T.; Yabashi, M.; Kubo, M.; Iwata, S.; Isobe, H.; Yamaguchi, K.; Suga, M.; Shen, J.-R. Oxygen-evolving photosystem II structures during S₁−S₂−S₃ transitions. *Nature* **2024**, *626*, 670−677.

(38) Dismukes, G.; Siderer, Y. EPR spectroscopic observations of a manganese center associated with water oxidation in spinach chloroplasts. *FEBS Lett.* **1980**, *121*, 78−80.

(39) Casey, J. L.; Sauer, K. EPR detection of a cryogenically photogenerated intermediate in photosynthetic oxygen evolution. *Biochim. Biophys. Acta Bioenerg.* **1984**, *767*, 21−28.

(40) Pantazis, D. A.; Ames, W.; Cox, N.; Lubitz, W.; Neese, F. Two interconvertible structures that explain the spectroscopic properties of the oxygen-evolving complex of photosystem II in the $S_2$ State. *Angew Chem. Int. Ed. Engl.* **2012**, *51*, 9935−9940.

(41) Vinyard, D. J.; Khan, S.; Askerka, M.; Batista, V. S.; Brudvig, G. W. Energetics of the $S_2$ state spin isomers of the oxygen-evolving complex of photosystem II. *J. Phys. Chem. B* **2017**, *121*, 1020−1025.

(42) Yang, K. R.; Lakshmi, K. V.; Brudvig, G. W.; Batista, V. S. Is deprotonation of the oxygen-evolving complex of photosystem II during the $S_1 \rightarrow S_2$ transitions suppressed by proton quantum delocalization? *J. Am. Chem. Soc.* **2021**, *143*, 8324−8332.

(43) Askerka, M.; Wang, J.; Vinyard, D. J.; Brudvig, G. W.; Batista, V. S. $S_3$ state of the $O_2$-evolving complex of photosystem II: Insights from QM/MM, EXAFS, and Femtosecond X-ray Diffraction. *Biochemistry* **2016**, *55*, 981−984.

(44) Li, X.; Siegbahn, P. E.; Ryde, U. Simulation of the isotropic EXAFS spectra for the $S_2$ and $S_3$ structures of the oxygen evolving complex in photosystem II. *Proc. Natl. Acad. Sci. U.S.A.* **2015**, *112*, 3979−3984.

(45) Isobe, H.; Shoji, M.; Shen, J.-R.; Yamaguchi, K. Chemical Equilibrium Models for the $S_3$ State of the Oxygen-Evolving Complex of Photosystem II. *Inorg. Chem.* **2016**, *55*, 502−511.

(46) Pantazis, D. A. The $S_3$ State of the Oxygen-Evolving Complex: Overview of Spectroscopy and XFEL Crystallography with a Critical Evaluation of Early-Onset Models for O−O Bond Formation. *Inorganics* **2019**, *7*, 55.

(47) Cox, N.; Retegan, M.; Neese, F.; Pantazis, D. A.; Boussac, A.; Lubitz, W. Electronic structure of the oxygen-evolving complex in photosystem II prior to O-O bond formation. *Science* **2014**, *345*, 804−808.

(48) Bovi, D.; Narzi, D.; Guidoni, L. The $S_2$ state of the oxygen-evolving complex of photosystem II explored by QM/MM dynamics: spin surfaces and metastable states suggest a reaction path towards the $S_3$ state. *Angew Chem. Int. Ed. Engl.* **2013**, *52*, 11744−11749.

(49) Mino, H.; Nagashima, H. Orientation of Ligand Field for Dangling Manganese in Photosynthetic Oxygen-Evolving Complex of Photosystem II. *J. Phys. Chem. B* **2020**, *124*, 128−133.

(50) Pushkar, Y.; K. Ravari, A.; Jensen, S. C.; Palenik, M. Early Binding of Substrate Oxygen Is Responsible for a Spectroscopically Distinct $S_2$ State in Photosystem II. *J. Phys. Chem. Lett.* **2019**, *10*, 5284−5291.

(51) Corry, T. A.; O'Malley, P. J. Proton Isomers Rationalize the High- and Low-Spin Forms of the $S_2$ State Intermediate in the Water-Oxidizing Reaction of Photosystem II. *J. Phys. Chem. Lett.* **2019**, *10*, 5226−5230.

(52) Corry, T. A.; O'Malley, P. J. Molecular Identification of a High-Spin Deprotonated Intermediate during the $S_2$ to $S_3$ Transition of Nature's Water-Oxidizing Complex. *J. Am. Chem. Soc.* **2020**, *142*, 10240−10243.

(53) Shoji, M.; Isobe, H.; Miyagawa, K.; Yamaguchi, K. Possibility of the right-opened Mn-oxo intermediate (R-oxo(4444)) among all nine intermediates in the $S_3$ state of the oxygen-evolving complex of photosystem II revealed by large-scale QM/MM calculations. *Chem. Phys.* **2019**, *518*, 81−90.

(54) Isobe, H.; Shoji, M.; Suzuki, T.; Shen, J.-R.; Yamaguchi, K. Exploring reaction pathways for the structural rearrangements of the Mn cluster induced by water binding in the $S_3$ state of the oxygen evolving complex of photosystem II. *J. Photochem. Photobiol., A* **2021**, *405*, 112905.

(55) Isobe, H.; Shoji, M.; Suzuki, T.; Shen, J.-R.; Yamaguchi, K. Roles of the Flexible Primary Coordination Sphere of the $Mn_4CaO_x$ Cluster: What Are the Immediate Decay Products of the $S_3$ State? *J. Phys. Chem. B* **2022**, *126*, 7212−7228.

(56) Guo, Y.; Messinger, J.; Kloo, L.; Sun, L. Reversible Structural Isomerization of Nature's Water Oxidation Catalyst Prior to O−O Bond Formation. *J. Am. Chem. Soc.* **2022**, *144*, 11736−11747.

(57) Guo, Y.; Messinger, J.; Kloo, L.; Sun, L. Alternative Mechanism for $O_2$ Formation in Natural Photosynthesis via Nucleophilic Oxo-Oxo Coupling. *J. Am. Chem. Soc.* **2023**, *145*, 4129−4141.

(58) Amin, M.; Kaur, D.; Yang, K. R.; Wang, J.; Mohamed, Z.; Brudvig, G. W.; Gunner, M. R.; Batista, V. Thermodynamics of the $S_2$-to-$S_3$ state transition of the oxygen-evolving complex of photosystem II. *Phys. Chem. Chem. Phys.* **2019**, *21*, 20840−20848.

(59) Suga, M.; Akita, F.; Yamashita, K.; Nakajima, Y.; Ueno, G.; Li, H.; Yamane, T.; Hirata, K.; Umena, Y.; Yonekura, S.; Yu, L.-J.; Murakami, H.; Nomura, T.; Kimura, T.; Kubo, M.; Baba, S.; Kumasaka, T.; Tono, K.; Yabashi, M.; Isobe, H.; Yamaguchi, K.; Yamamoto, M.; Ago, H.; Shen, J.-R. An oxyl/oxo mechanism for oxygen-oxygen coupling in PSII revealed by an x-ray free-electron laser. *Science* **2019**, *366*, 334−338.

(60) Wang, J. Active-site omit maps reveal a $CaMn_4O_5$ composition for two-flash advanced water oxidase. *Science* **2020**. E-letter.

(61) Wang, J.; Armstrong, W. H.; Batista, V. S. Do crystallographic XFEL data support binding of a water molecule to the oxygen-evolving complex of photosystem II exposed to two flashes of light? *Proc. Natl. Acad. Sci. U.S.A.* **2021**, *118*, No. e2023982118.

(62) Ibrahim, M.; Moriarty, N. W.; Kern, J.; Holton, J. M.; Brewster, A. S.; Bhowmick, A.; Bergmann, U.; Zouni, A.; Messinger, J.; Yachandra, V. K.; Yano, J.; Dobbek, H.; Sauter, N. K.; Adams, P. D. Reply to Wang et al.: Clear evidence of binding of Ox to the oxygen-evolving complex of photosystem II is best observed in the omit map. *Proc. Natl. Acad. Sci. U.S.A.* **2021**, *118*, No. e2102342118.

(63) Drosou, M.; Comas-Vilà, G.; Neese, F.; Salvador, P.; Pantazis, D. A. Does Serial Femtosecond Crystallography Depict State-Specific Catalytic Intermediates of the Oxygen-Evolving Complex? *J. Am. Chem. Soc.* **2023**, *145*, 10604−10621.

(64) Wang, J.; Gisriel, C. J.; Reiss, K.; Huang, H.-L.; Armstrong, W. H.; Brudvig, G. W.; Batista, V. S. Heterogeneous Composition of Oxygen-Evolving Complexes in Crystal Structures of Dark-Adapted Photosystem II. *Biochemistry* **2021**, *60*, 3374−3384.

(65) Ames, W.; Pantazis, D. A.; Krewald, V.; Cox, N.; Messinger, J.; Lubitz, W.; Neese, F. Theoretical evaluation of structural models of the $S_2$ state in the oxygen evolving complex of photosystem II: protonation states and magnetic interactions. *J. Am. Chem. Soc.* **2011**, *133*, 19743−19757.

(66) Wang, J.; Askerka, M.; Brudvig, G. W.; Batista, V. S. Crystallographic data support the carousel mechanism of water supply to the oxygen-evolving complex of photosystem II. *ACS Energy Lett.* **2017**, *2*, 2299−2306.

(67) Guo, Y.; Li, H.; He, L.-L.; Zhao, D.-X.; Gong, L.-D.; Yang, Z.-Z. The open-cubane oxo−oxyl coupling mechanism dominates photosynthetic oxygen evolution: a comprehensive DFT investigation on O−O bond formation in the $S_4$ state. *Phys. Chem. Chem. Phys.* **2017**, *19*, 13909−13923.

(68) Siegbahn, P. E. M. The $S_2$ to $S_3$ Transition for water oxidation in PSII (photosystem II), revisited. *Phys. Chem. Chem. Phys.* **2018**, *20*, 22926−22931.

(69) Allgöwer, F.; Gamiz-Hernandez, A. P.; Rutherford, A. W.; Kaila, V. R. I. Molecular principles of redox-coupled protonation dynamics in photosystem II. *J. Am. Chem. Soc.* **2022**, *144*, 7171−7180.

(70) Klauss, A.; Haumann, M.; Dau, H. Seven steps of alternating electron and proton transfer in photosystem II water oxidation traced by time-resolved photothermal beam deflection at improved sensitivity. *J. Phys. Chem. B* **2015**, *119*, 2677−2689.

(71) T. Babcock, G.; Blankenship, R. E.; Sauer, K. Reaction kinetics for positive charge accumulation on the water side of chloroplast photosystem II. *FEBS Lett.* **1976**, *61* (2), 286−289.

(72) Ugur, I.; Rutherford, A. W.; Kaila, V. R. Redox-coupled substrate water reorganization in the active site of Photosystem II-The role of calcium in substrate water delivery. *Biochim. Biophys. Acta* **2016**, *1857*, 740−748.

(73) Kim, C. J.; Debus, R. J. One of the Substrate Waters for $O_2$ Formation in Photosystem II Is Provided by the Water-Splitting $Mn_4CaO_5$ Cluster's $Ca^{2+}$ Ion. *Biochemistry* **2019**, *58*, 3185−3192.

(74) Ghosh, I.; Banerjee, G.; Kim, C. J.; Reiss, K.; Batista, V. S.; Debus, R. J.; Brudvig, G. W. D1-S169A substitution of photosystem II perturbs water oxidation. *Biochemistry* **2019**, *58*, 1379−1387.

(75) Ghosh, I.; Banerjee, G.; Reiss, K.; Kim, C. J.; Debus, R. J.; Batista, V. S.; Brudvig, G. W. D1-S169A substitution of photosystem II reveals a novel $S_2$-state structure. *Biochim. Biophys. Acta Bioenerg.* **2020**, *1861*, 148301.

(76) Amin, M.; Vogt, L.; Szejgis, W.; Vassiliev, S.; Brudvig, G. W.; Bruce, D.; Gunner, M. R. Proton-Coupled Electron Transfer During the S-State Transitions of the Oxygen-Evolving Complex of Photosystem II. *J. Phys. Chem. B* **2015**, *119*, 7366−7377.

(77) Tagore, R.; Crabtree, R. H.; Brudvig, G. W. Distinct Mechanisms of Bridging-Oxo Exchange in Di-*μ*-O Dimanganese Complexes with and without Water-Binding Sites: Implications for Water Binding in the $O_2$-Evolving Complex of Photosystem II. *Inorg. Chem.* **2007**, *46*, 2193−2203.

(78) Boussac, A.; Ugur, I.; Marion, A.; Sugiura, M.; Kaila, V. R.; Rutherford, A. W. The low spin - high spin equilibrium in the $S_2$-state of the water oxidizing enzyme. *Biochim. Biophys. Acta Bioenerg.* **2018**, *1859*, 342−356.

(79) Haumann, M.; Müller, C.; Liebisch, P.; Iuzzolino, L.; Dittmer, J.; Grabolle, M.; Neisius, T.; Meyer-Klaucke, W.; Dau, H. Structural and Oxidation State Changes of the Photosystem II Manganese Complex in Four Transitions of the Water Oxidation Cycle ($S_0 \rightarrow S_1$, $S_1 \rightarrow S_2$, $S_2 \rightarrow S_3$, and $S_{3,4} \rightarrow S_0$) Characterized by X-ray Absorption Spectroscopy at 20 K and Room Temperature. *Biochemistry* **2005**, *44*, 1894−1908.

(80) Vassiliev, S.; Zaraiskaya, T.; Bruce, D. Exploring the energetics of water permeation in photosystem II by multiple steered molecular dynamics simulations. *Biochim. Biophys. Acta* **2012**, *1817*, 1671−1678.

(81) Boussac, A.; Kuhl, H.; Un, S.; Rögner, M.; Rutherford, A. W. Effect of Near-Infrared Light on the $S_2$-State of the Manganese Complex of Photosystem II from *Synechococcus elongatus*. *Biochemistry* **1998**, *37*, 8995−9000.

(82) Pokhrel, R.; Brudvig, G. W. Oxygen-evolving complex of photosystem II: correlating structure with spectroscopy. *Phys. Chem. Chem. Phys.* **2014**, *16*, 11812−11821.

(83) Askerka, M.; Vinyard, D. J.; Wang, J.; Brudvig, G. W.; Batista, V. S. Analysis of the Radiation-Damage-Free X-ray Structure of Photosystem II in Light of EXAFS and QM/MM Data. *Biochemistry* **2015**, *54*, 1713−1716.